J. Fluid Mech. (2012), *vol.* 711, *pp.* 212–258.
doi:10.1017/jfm.2012.388

Streamwise dispersion and mixing in quasi-two-dimensional steady turbulent jets

Julien R. Landel[1,2]†, C. P. Caulfield[1,2] and Andrew W. Woods[1]

[1] BP Institute, University of Cambridge, Madingley Road, Cambridge CB3 0EZ, UK

[2] Department of Applied Mathematics and Theoretical Physics, University of Cambridge, Centre for Mathematical Sciences, Wilberforce Road, Cambridge CB3 0WA, UK

(Received 28 February 2012; revised 27 June 2012; accepted 28 July 2012; first published online 12 September 2012)

We investigate experimentally and theoretically the streamwise transport and dispersion properties of steady quasi-two-dimensional plane turbulent jets discharged vertically from a slot of width d into a fluid confined between two relatively close rigid boundaries with gap $W \sim O(d)$. We model the evolution in time and space of the concentration of passive tracers released in these jets using a one-dimensional time-dependent effective advection–diffusion equation. We make a mixing length hypothesis to model the streamwise turbulent eddy diffusivity such that it scales like $b(z)\overline{w}_m(z)$, where z is the streamwise coordinate, b is the jet width, $\overline{w}_m$ is the maximum time-averaged vertical velocity. Under these assumptions, the effective advection–diffusion equation for $\phi(z,t)$, the horizontal integral of the ensemble-averaged concentration, is of the form $\partial_t\phi + K_a {M_0}^{1/2}\partial_z\left(\phi/z^{1/2}\right) = K_d {M_0}^{1/2}\partial_z\left(z^{1/2}\partial_z\phi\right)$, where t is time, K_a (the advection parameter) and K_d (the dispersion parameter) are empirical dimensionless parameters which quantify the importance of advection and dispersion, respectively, and M_0 is the source momentum flux. We find analytical solutions to this equation for ϕ in the cases of a constant-flux release and an instantaneous finite-volume release. We also give an integral formulation for the more general case of a time-dependent release, which we solve analytically when tracers are released at a constant flux over a finite period of time. From our experimental results, whose concentration distributions agree with the model, we find that $K_a = 1.65 \pm 0.10$ and $K_d = 0.09 \pm 0.02$, for both finite-volume releases and constant-flux releases using either dye or virtual passive tracers. The experiments also show that streamwise dispersion increases in time as $t^{2/3}$. As a result, in the case of finite-volume releases more than 50 % of the total volume of tracers is transported ahead of the purely advective front (i.e. the front location of the tracer distribution if all dispersion mechanisms are ignored and considering a 'top-hat' mean velocity profile in the jet); and in the case of constant-flux releases, at each instant in time, approximately 10 % of the total volume of tracers is transported ahead of the advective front.

Key words: jets, mixing and dispersion, shallow water flows

1. Introduction

In the event of a spill of pollutants, waste or any other tracers into a river, it is crucial to predict how the tracers are advected and dispersed by the flow after they

† Email address for correspondence: jl501@cam.ac.uk

reach a relatively shallow basin, such as a lake or the sea shelf. Such predictions can be used to monitor the spread of the tracers, control their impact on the environment and assess any potential damage. One of the most important aspects of these shallow river flows, and one which has raised the interest of scientists for more than 20 years, is the emergence of large-scale eddy structures and meanders at some distance away from the river mouth. These eddies and meanders have been visualized in nature on several occasions due to sediments transported by the flow (see e.g. Giger, Dracos & Jirka 1991; Jirka & Uijttewaal 2004; Rowland, Stacey & Dietrich 2009). Giger *et al.* (1991) were interested in the entrainment and mixing in shallow water flows, whose characteristic horizontal dimensions were much larger than the fluid-layer thickness and where the flow developed in a confined environment. They showed that these geophysical flows could be reproduced in laboratory experiments by confining plane turbulent jets in the spanwise direction (i.e. the direction parallel to the line source of the jet). Giger *et al.* (1991) observed that in the far field, or for $z/W > 10$ where z is the spatial coordinate in the streamwise direction and W is the fluid-layer thickness in the spanwise direction (i.e. W corresponded to the depth of the basin), the jet produced similar large eddies and meanders as observed in shallow river flows. In Landel, Caulfield & Woods (2012), we referred to turbulent plane jets in such a confined geometry in the far field as quasi-two-dimensional jets. The present work is focused on the advection and dispersion properties of such quasi-two-dimensional jets, particularly when considering the transport of a passive scalar.

The essential characteristics of quasi-two-dimensional jets have been described previously. Dracos, Giger & Jirka (1992) showed that the large planar counter-rotating eddies observed in quasi-two-dimensional jets developed due to an inverse cascade of quasi-two-dimensional turbulence. Chen & Jirka (1998) proved through linear stability analysis that the meanders of the jet were the result of a sinuous instability. According to Jirka & Uijttewaal (2004) the sinuous instability of the jet originated from internal transverse shear across the jet. In Landel *et al.* (2012), we showed that the time-averaged velocity field of quasi-two-dimensional jets could be modelled using two-dimensional plane jet theory. We also studied the instantaneous velocity field and revealed the interactions between the high-speed meandering core of the jet and the large eddies alternating on its sides. We showed that these core and eddy structures were self-similar with distance and continuously exchanged fluid between themselves, as well as with the ambient fluid surrounding the jet. In particular, the eddies played a key role in the entrainment of ambient fluid by means of engulfment at their rear. Entrained fluid could either be trapped for a brief period in an eddy, where it experienced strong mixing, or be directly incorporated in the core of the jet, where it was advected downstream much more rapidly. We further hypothesized that because of the difference in advection speed between the core and the eddies (we measured that on average eddies travelled at approximately $1/4$ of the speed of the core), initially relatively close fluid parcels entrained by the jet should experience large streamwise dispersion depending on whether they were drawn into the eddies or the core.

In order to study and model the transport, mixing and dispersion of tracers in shallow river flows, we investigate the temporal and spatial evolution of the concentration of tracers released in quasi-two-dimensional jets. The mixing properties of turbulent jets have been studied experimentally many times. Uberoi & Singh (1975) measured instantaneous temperature profiles in plane jets and found that they differed from typical time-averaged Gaussian profiles. They reported a relatively well-mixed interior while most of the mixing was performed at the turbulent–non-turbulent interface of the jet. Schefer *et al.* (1994) also noted a difference between the

instantaneous distribution and the time-averaged distribution of tracers in the case of three-dimensional round turbulent jets. They attributed this discrepancy to the development of large-scale vortical structures. Arguably, the dynamics of large-scale vortical structures is different in quasi-two-dimensional jets from the case of three-dimensional round or plane jets due to the confinement of the flow in one direction; see Jirka (2001) for a discussion on large-scale flow structures in shallow flows, or Landel *et al.* (2012) for quasi-two-dimensional jets specifically. Nevertheless, large-scale vortical structures do have an influence on the mixing and dilution properties of quasi-two-dimensional jets. Giger *et al.* (1991) reported that mixing efficiency and dilution in quasi-two-dimensional jets tended to diminish with distance. From turbulence spectral analysis and intermittency analysis, Dracos *et al.* (1992) argued that the decrease of mixing efficiency was due to the development of quasi-two-dimensional turbulence. Using laser-induced fluorescence in quasi-two-dimensional jets, Chen & Jirka (1999) showed that quasi-two-dimensional turbulence induced patchiness in the time-dependent distribution of the tracer concentration. They found distinct regions of large concentration which corresponded to the large-scale turbulent structures. Jirka (2001) reflected upon the impact of large vortical structures in shallow river flows and emphasized their ability to transport relatively unmixed fluid over large distances.

Dispersion in shear flows was first studied by Taylor (1953) for a laminar flow in a pipe and then for a turbulent flow in a pipe (Taylor 1954). As discussed in the review of Fischer (1973), the model developed in Taylor (1953, 1954), which is that lateral shear can induce streamwise dispersion, was then applied to open channel flows, such as the flow in estuaries. Fischer (1973) reported measurements of the diffusion coefficient as a function of the transverse velocity gradient for both laboratory experiments and field measurements (see e.g. Ward & Fischer 1971). In his conclusion, Fischer (1973) pointed out the lack of theoretical models for open channel flows. Chatwin & Allen (1985) reviewed the work on dispersion in rivers and estuaries. They detailed the various nonlinear and non-stationary physical mechanisms which can affect transport and dispersion in rivers and estuaries, and described past theoretical and experimental work addressing these issues. They also discussed the shortcomings of using (relatively short) time-averaged quantities (measured in field work) instead of true ensemble-averaged quantities in the modelling of time-dependent transport and dispersion. In their conclusion, Chatwin & Allen (1985) urged that 'more well-designed laboratory experiments' be conducted to complement theoretical modelling and field measurements. Lewis (1997) gave a clear mathematical description of the fundamental physical processes, such as shear dispersion and turbulent mixing, and how they can be applied to the complex case of dispersion in estuaries. The latest research advances about dispersion in rivers and estuaries are summarized in MacCready & Geyer (2010).

Despite the large number of experimental studies, there appear to have been relatively few attempts to provide a comprehensive model of the advection and dispersion processes in quasi-two-dimensional jets. Moreover, most models assume a steady state. Paranthoën *et al.* (1988) suggested a limited model for the initial phase of the dispersion process in a turbulent plane jet. Then, from conservation of mass in a classical plane jet, Chen & Jirka (1999) showed that the decay of the time-averaged concentration of passive tracers $\overline{C}$ along the centreline of quasi-two-dimensional jets followed $\overline{C} \propto z^{-1/2}$. Using conservation of mass and the Reynolds-averaged Navier–Stokes equation with the boundary-layer approximation for three-dimensional round and plane jets, Law (2006) proposed an analytic solution for the

time-averaged concentration distribution across the jet. To close the problem, he used the common assumption that the turbulent diffusive term was proportional to the gradient of the time-averaged concentration across the jet. He also assumed that the coefficient of proportionality between these two quantities (the turbulent diffusivity) was constant across the jet and depended only on the eddy diffusivity and the turbulent Schmidt number; see e.g. Mathieu & Scott (2000) for more details.

Previous models often assume purely lateral entrainment, and then simple time-averaged streamwise motion. Owing to the cross-stream variation in along-stream velocity (due to the time-dependent core–eddy interaction and the time-averaged Gaussian streamwise velocity distribution) quasi-two-dimensional jets inevitably have significant along-stream dispersion. We want to investigate the implications of this along-stream dispersion for tracer transport and how it affects advection in quasi-two-dimensional jets.

In this paper, we propose a new one-dimensional model solving the time-dependent effective advection–diffusion equation along the direction of the flow, based on mixing-length theory. Mixing-length theory is appropriate because of the central role of large eddies (scaling with the local jet width) on the dispersion within the flow. We find analytical solutions in similarity form for the case of a constant-flux release and the case of a finite-volume release of tracers, which appear to describe correctly some new experimental measurements of tracer transport. We are able to formulate the general solution for any time-dependent release in integral form, effectively by means of a Green's-function-like solution. We also show the importance of along-stream dispersion mechanisms in quasi-two-dimensional jets, by comparing our full effective advection–diffusion model with a simple advection model. In § 2 we present our model hypothesis starting from the advection–diffusion equation, where the diffusive term models the dispersion by the turbulent flow field of quasi-two-dimensional jets. In § 3 we derive analytical solutions for both a constant volume-flux release and an instantaneous finite-volume release. We also show how to generalize the analytical solution for an instantaneous finite-volume release into a solution for an arbitrary time-dependent release. In § 4 we describe our experimental procedure. In § 5 we first provide a qualitative assessment of our model hypothesis, then we compare our theoretical predictions with experimental data obtained using dye tracking experiments and complementary virtual particle tracking experiments in both the constant-flux and the finite-volume cases. Finally, in § 6 we draw our conclusions.

2. Turbulent model hypothesis

To characterize the evolution of the concentration of tracers released in quasi-two-dimensional jets, we consider the ideal model of a turbulent momentum jet in a two-dimensional semi-infinite environment. Adopting the same conventions as Landel *et al.* (2012), the flow is considered incompressible and statistically steady. The x-direction is the lateral, cross-jet or horizontal direction and the z-direction is the streamwise, axial or vertical direction. Assuming a plane flow in the domain, the velocity is labelled $\boldsymbol{u} = (u, w)$ in a Cartesian coordinate system (x, z) with the origin at the nozzle exit.

We consider the statistical effect of quasi-two-dimensional turbulence on the concentration $C(x, z, t)$ (where t is time) of passive tracers in the jet flow. We believe that, on average, the interaction between the high-speed core and the growing eddies has a strong streamwise dispersive effect. On the other hand, the horizontal (or cross-jet) distribution of the tracer concentration remains, on average, confined laterally by

the linearly-expanding straight-sided boundaries of the jet. We found in Landel *et al.* (2012) that the average dye edges of quasi-two-dimensional dyed jets expand linearly with streamwise distance: we discuss this point further in § 5.2. As we have already mentioned, the transport and dispersion of tracers in quasi-two-dimensional jets is more critical in the streamwise direction (Jirka 2001). Therefore, we choose to study the ensemble-averaged horizontally-integrated concentration

$$\phi(z,t) = \int_{-\infty}^{\infty} C_{\mathrm{E}}(x,z,t)\,\mathrm{d}x, \tag{2.1}$$

where the ensemble-averaged concentration is defined as

$$C_{\mathrm{E}}(x,z,t) = \frac{1}{N}\sum_{n=1}^{N} C_n(x,z,t), \tag{2.2}$$

where N is the total number of realizations of an experiment and n designates the nth realization.

Neglecting molecular diffusion under the assumption that it is less significant than eddy diffusion processes (Mathieu & Scott 2000), we propose a heuristic equation for the time-dependent transport and dispersion of the ensemble-averaged horizontally-integrated concentration

$$\partial_t\phi + \partial_z M_\phi = k_d\partial_z(b\overline{w}_m\,\partial_z\phi), \quad M_\phi = k_a\overline{w}_m\phi, \tag{2.3a,b}$$

where M_ϕ is the vertical (streamwise) concentration flux of tracers, k_a and k_d are two empirical constants of proportionality, $b(z)$ is the jet velocity width or e-folding distance of the time-averaged vertical velocity at height z, and $\overline{w}_m(z)$ is the maximum time-averaged vertical velocity in the jet at height z. Landel *et al.* (2012) found

$$b(z) = \frac{{Q_0}^2}{\sqrt{2\pi}M_0}\left(4\sqrt{2}\alpha\frac{M_0 z}{{Q_0}^2}+1\right) \quad \text{and} \quad \overline{w}_m(z) = \frac{\sqrt{2}M_0}{Q_0}\left(4\sqrt{2}\alpha\frac{M_0 z}{{Q_0}^2}+1\right)^{-1/2}, \tag{2.4a,b}$$

where α is the entrainment coefficient (Morton, Taylor & Turner 1956), Q_0 is the initial volume flux of the jet, and M_0 is the initial momentum flux, which is conserved with distance in the z-direction (see Landel *et al.* 2012). In the one-dimensional time-dependent effective advection–diffusion equation (2.3), we assume that advection is governed by the mean flow, with characteristic velocity proportional to $\overline{w}_m$, i.e. $k_a\overline{w}_m$. Moreover, we assume that dispersion is governed by eddy processes and lateral shear (similarly to Taylor dispersion in turbulent shear flows: Taylor 1954), such that the eddy diffusion coefficient scales like the local characteristic velocity $\overline{w}_m(z)$ and the local characteristic size $b(z)$ of the core and eddy structure of the jet. This is analogous to a 'mixing-length' model (Prandtl 1925), where the mixing length is the local characteristic width of the jet, and where streamwise transport and dispersion are dominant.

The quantities b and $\overline{w}_m$ can be rewritten in power-law form using (2.4*a*) and (2.4*b*) (neglecting the virtual origins, i.e. considering an ideal point source for the jet) respectively, to obtain the effective advection–diffusion equation for the horizontally-integrated ensemble-averaged concentration ϕ,

$$\partial_t\phi + \partial_z M_\phi = K_d {M_0}^{1/2}\,\partial_z\left(z^{1/2}\partial_z\phi\right), \quad M_\phi = K_a {M_0}^{1/2}\frac{\phi}{z^{1/2}}, \tag{2.5a,b}$$

where the constants K_a and K_d are a dimensionless advection parameter and a dimensionless dispersion parameter, respectively, which we will determine experimentally. The parameters K_a and K_d can be related to k_a and k_d using (2.4*a*) and (2.4*b*) if we, again, neglect the virtual origins

$$K_a = \frac{k_a}{\left(2\alpha\sqrt{2}\right)^{1/2}} \quad \text{and} \quad K_d = 2k_d\left(\frac{\alpha\sqrt{2}}{\pi}\right)^{1/2}, \tag{2.6a,b}$$

with $\alpha \approx 0.068$ (Landel *et al.* 2012). It is interesting to note that in (2.5) the dispersion term increases with distance like $z^{1/2}$, whereas the advection term decreases with distance like $z^{-1/2}$.

3. Mathematical model

In order to test our turbulent model hypothesis, we impose different, appropriate initial, boundary and integral conditions on solutions to the general effective advection–diffusion equation (2.5), for example,

$$\phi(z, 0) = 0 \quad \text{for } z > 0, \quad \phi(z, t) \to 0 \quad \text{as } z \to \infty \quad \text{and} \tag{3.1a,b}$$

$$\int_0^\infty \phi(z, t)\,\mathrm{d}z \propto t^{\vartheta} \quad \text{for } t > 0. \tag{3.1c}$$

Equation (3.1*a*) imposes that the concentration is zero everywhere initially; (3.1*b*) imposes that, at all time, the concentration vanishes at infinity; and (3.1*c*) imposes that, for $t > 0$, the total integrated concentration evolves as a power law of time. The integral condition (3.1*c*) effectively controls the release of the passive tracers in the jet.

In this theoretical section, we solve (2.5) analytically for three different sets of initial boundary and integral conditions. We consider the simple case of a constant-flux release of passive tracers (i.e. we impose $\vartheta = 1$ in (3.1*c*)), which we solve by analysing either the concentration (see § 3.2) or the concentration flux (see § 3.3). In the second case, presented in § 3.4, we consider an instantaneous release of a finite volume of passive tracers at the origin of the jet (i.e. we impose $\vartheta = 0$ in (3.1*c*)). Then, based on the solution for the instantaneous finite-volume release, in § 3.5 we show how to formulate, in integral form, the solution for a general and more realistic time-dependent release of tracers governed by a source function, which has an arbitrary time dependence, using a Green's function approach. We give an analytical solution in the case where the source function models a constant-flux release over a finite period of time T_0. We further show that the solutions for the first two simpler cases of a constant-flux release and an instantaneous finite-volume release are the two asymptotic limits of the more general solution when $T_0 \to \infty$ and $t \gg T_0$, respectively.

We choose to solve the problems of a constant-flux release and a finite-volume release because we can reproduce them experimentally, and thus test our turbulent model hypothesis and the various associated assumptions, stated in § 2, against experimental measurements (presented in § 5). Before deriving the solutions of the three cases, we use below a similarity transformation to simplify the partial differential equation (2.5) into an ordinary differential equation (ODE), which we can then solve.

3.1. *Similarity transformation*

We introduce the dilation transformation

$$\check{z} = \varepsilon^a z, \quad \check{t} = \varepsilon^b t, \quad \check{\phi} = \varepsilon^c \phi(\varepsilon^{-a}\check{z}, \varepsilon^{-b}\check{t}), \tag{3.2}$$

and so (2.5) becomes

$$\varepsilon^{b-c}\partial_{\check{t}}\check{\phi} + \varepsilon^{(3/2)a-c}K_a {M_0}^{1/2}\,\partial_{\check{z}}\left(\frac{\check{\phi}}{\check{z}^{1/2}}\right) = \varepsilon^{(3/2)a-c}K_d {M_0}^{1/2}\,\partial_{\check{z}}\left(\check{z}^{1/2}\partial_{\check{z}}\check{\phi}\right). \tag{3.3}$$

If $b = 3a/2$, then (2.5) is invariant under this transformation. This suggests that we look for a solution for (2.5) of the form

$$\phi(z,t) = t^{2c/(3a)}\,y(\eta) \quad \text{with } \eta = \frac{z}{t^{2/3}{M_0}^{1/3}}. \tag{3.4}$$

Thus (2.5) becomes

$$\left(\frac{2c}{3a} - \frac{K_a}{2\eta^{3/2}}\right)y + \left(\frac{(2K_a - K_d)}{2\eta^{1/2}} - \frac{2\eta}{3}\right)y' - K_d\eta^{1/2}y'' = 0. \tag{3.5}$$

The general effective advection–diffusion problem has thus been simplified to the ODE (3.5). This second-order ODE, written in similarity form, captures both the temporal and spatial streamwise evolution of the concentration of tracers in a quasi-two-dimensional steady turbulent jet. Most importantly, (3.5) allows not only for streamwise advection transport, but also for streamwise turbulent dispersion. Furthermore, we can note that the time evolution implicit in (3.5) depends on the ratio of two dilation constants, c/a. This ratio can be determined using the integral condition for conservation of concentration (3.1*c*), which becomes, using (3.4), for $t > 0$

$$\int_0^\infty \phi(z,t)\,\mathrm{d}z = t^{2c/(3a)}\int_0^\infty y\left(\frac{z}{t^{2/3}}\right)t^{2/3}{M_0}^{1/3}\mathrm{d}\eta = {M_0}^{1/3}t^{(2c/(3a)+2/3)}\int_0^\infty y(\eta)\,\mathrm{d}\eta \propto t^{\vartheta}. \tag{3.6}$$

Therefore, this condition can hold for all $t > 0$ if and only if

$$\frac{c}{a} = \frac{3\vartheta - 2}{2}. \tag{3.7}$$

3.2. *Constant-flux release: concentration*

In the case of a release of tracers at a constant source flux F, if the general effective advection–diffusion equation (2.5) is satisfied for $z > 0$, $t > 0$ and if, in addition, $\phi(z,t)$ satisfies (following (3.1*a–c*) with $\vartheta = 1$)

$$\phi(z,0) = 0 \quad \text{for } z > 0, \quad \phi(z,t) \to 0 \quad \text{as } z \to \infty \quad \text{and} \quad \int_0^\infty \phi(z,t)\,\mathrm{d}z = Ft \quad \text{for } t > 0, \tag{3.8a–c}$$

then the condition (3.8*c*) can hold for all $t > 0$ if and only if $a = 2c$ according to (3.7) with $\vartheta = 1$. Thus, (3.4) becomes

$$\phi(z,t) = t^{1/3}y(\eta) \quad \text{with } \eta = \frac{z}{t^{2/3}{M_0}^{1/3}}. \tag{3.9}$$

In this case, the initial boundary value problem for $\phi(z,t)$, defined by (3.5) with $a = 2c$, (3.8*a–c*) and (3.9), reduces to

$$\left(\frac{1}{3} - \frac{K_a}{2\eta^{3/2}}\right)y + \left(\frac{(2K_a - K_d)}{2\eta^{1/2}} - \frac{2\eta}{3}\right)y' - K_d\eta^{1/2}y'' = 0, \tag{3.10}$$

subject to the conditions

$$y(\eta) \to 0 \quad \text{as } \eta \to \infty, \qquad \int_0^\infty y(\eta)\,\mathrm{d}\eta = \frac{F}{{M_0}^{1/3}} \quad \text{for } t > 0. \tag{3.11a,b}$$

Equation (3.10) can then be rewritten using

$$y(\eta) = s^{1/3(K_a/K_d-1)} p(s) \quad \text{with } s = \frac{4\eta^{3/2}}{9K_d}, \tag{3.12}$$

to obtain

$$p'' + p' + \left(\frac{\frac{1}{3}\left(\frac{K_a}{K_d} - 2\right)}{s} + \frac{\frac{1}{4} - \left(\frac{1}{3}\left(\frac{K_a}{K_d} - \frac{1}{2}\right)\right)^2}{s^2} \right) p = 0. \tag{3.13}$$

Making the change of variable $p = \mathrm{e}^{-s/2} W$, we obtain the Whittaker differential equation (Gradshteyn & Ryzhik 2007). The Whittaker functions $W_{k,m}[s]$ and $M_{k,m}[s]$ are two linearly independent solutions of the Whittaker differential equation, where

$$k = \frac{1}{3}\left(\frac{K_a}{K_d} - 2\right), \quad m = \frac{1}{3}\left(\frac{K_a}{K_d} - \frac{1}{2}\right). \tag{3.14a,b}$$

Therefore, the solution of (3.13) is

$$p(s) = \mathrm{e}^{-s/2}(J_W W_{k,m} + J_M M_{k,m})[s], \tag{3.15}$$

where J_W and J_M are constants of integration which will be determined using the boundary conditions (3.11*a,b*). We can rewrite (3.15) in the similarity form

$$y(\eta) = \left(\frac{4\eta^{3/2}}{9K_d}\right)^{1/3(K_a/K_d-1)} \mathrm{e}^{-\left(2\eta^{3/2}/9K_d\right)} (J_W W_{k,m} + J_M M_{k,m}) \left[\frac{4\eta^{3/2}}{9K_d}\right] = J_W \mathscr{W} + J_M \mathscr{M}, \tag{3.16}$$

defining two linearly independent solutions: $\mathscr{W}$ (involving $W_{k,m}$), and $\mathscr{M}$ (involving $M_{k,m}$) of the underlying equation (3.15). Since $m - k - 1/2 = 0$, we can actually simplify the Whittaker functions $W_{k,m}$ and $M_{k,m}$ (see equations (13.18.5) and (13.18.4) for $W_{m-1/2,m}$ and $M_{m-1/2,m}$, respectively, in the National Institute of Standards and Technology *Digital Library of Standards and Technology* (NIST 2012)),

$$\mathscr{W}(\eta) = \left(\frac{4\eta^{3/2}}{9K_d}\right)^{1/3} \Gamma\left[\frac{2}{3}\left(\frac{K_a}{K_d} - \frac{1}{2}\right), \frac{4\eta^{3/2}}{9K_d}\right], \tag{3.17}$$

$$\mathscr{M}(\eta) = \frac{2}{3}\left(\frac{K_a}{K_d} - \frac{1}{2}\right)\left(\frac{4\eta^{3/2}}{9K_d}\right)^{1/3} \gamma\left[\frac{2}{3}\left(\frac{K_a}{K_d} - \frac{1}{2}\right), \frac{4\eta^{3/2}}{9K_d}\right], \tag{3.18}$$

where $\Gamma[g,\zeta] = \int_\zeta^\infty h^{g-1}\mathrm{e}^{-h}\,\mathrm{d}h$ is the upper incomplete gamma function and $\gamma[g,\zeta] = \int_0^\zeta h^{g-1}\mathrm{e}^{-h}\,\mathrm{d}h$ is the lower incomplete gamma function. We can prove that, as $\eta \to \infty$,

$$\mathscr{W}(\eta \to \infty) \sim \mathrm{e}^{-\eta^{3/2}} \eta^{(K_a/K_d - 3/2)}, \quad \mathscr{M}(\eta \to \infty) \sim \eta^{1/2}, \tag{3.19a,b}$$

(see equation (8.11.2) in NIST 2012 for the asymptotic expansion of the upper incomplete gamma function) for $K_a > K_d/2$. We will find later that for our

experimental data K_a appears to be substantially greater than K_d, which is consistent with this requirement. In order to satisfy the far-field boundary condition (3.11*a*) requiring decay of y, $J_M = 0$ so that the solution depends on $\mathscr{W}$ alone. J_W can then be determined using the boundary condition (3.11*b*):

$$J_W = \frac{F}{{M_0}^{1/3}\displaystyle\int_0^\infty \mathscr{W}(\eta)\,\mathrm{d}\eta}. \tag{3.20}$$

Therefore, the general solution of the effective advection–diffusion problem for the case of a constant-flux release at the source is, in similarity form, for $K_a > K_d/2$

$$y_F(\eta) = \frac{2F}{3K_d{M_0}^{1/3}\Gamma\left[\dfrac{2}{3}\left(\dfrac{K_a}{K_d}+1\right)\right]}\eta^{1/2}\Gamma\left[\frac{2}{3}\left(\frac{K_a}{K_d}-\frac{1}{2}\right), \frac{4\eta^{3/2}}{9K_d}\right], \tag{3.21}$$

where $\Gamma[g] = \int_0^\infty h^{g-1}\mathrm{e}^{-h}\,\mathrm{d}h$ is the gamma function.

Interestingly, in the purely advective limit where $K_d \to 0$, corresponding to a so-called 'top-hat' mean velocity profile in the jet (see e.g. Turner 1986) with no turbulent dispersion parametrized, (3.10) becomes

$$\left(\frac{1}{3}-\frac{K_a}{2\eta^{3/2}}\right)y + \left(\frac{K_a}{\eta^{1/2}}-\frac{2\eta}{3}\right)y' = 0, \tag{3.22}$$

which integrates to

$$y_{F,a}(\eta) = \begin{cases} J_1\eta^{1/2}, & 0 \leqslant \eta < \eta_a, \\ J_2\eta^{1/2}, & \eta_a < \eta, \end{cases} \tag{3.23}$$

where J_1 and J_2 are integration constants, and

$$\eta_a = \left(\frac{3K_a}{2}\right)^{2/3} \tag{3.24}$$

is the location of the advective front considering 'top-hat' mean velocity profiles in the jet. Using the boundary condition at infinity (3.11*a*), we obtain $J_2 = 0$. J_1 can be determined using the integral condition (3.11*b*). Therefore, the similarity solution of the purely advective problem for the case of a constant-flux release at the source is

$$y_{F,a}(\eta) = \begin{cases} \dfrac{F}{K_a{M_0}^{1/3}}\eta^{1/2}, & 0 \leqslant \eta < \eta_a, \\ 0, & \eta_a < \eta. \end{cases} \tag{3.25}$$

We have plotted the non-dimensional quantities $y_F/\left(F/{M_0}^{1/3}\right)$ and $y_{F,a}/\left(F/{M_0}^{1/3}\right)$ as functions of the similarity variable $\eta = z/\left(t^{2/3}{M_0}^{1/3}\right)$ in figure 1. The five different curves show the concentration profile in similarity form for different values of K_a and K_d. As we increase K_a (determining the advection strength), the maximum of the curve is displaced upwards, further away from the origin, while if we increase K_d (determining the dispersion strength), the front drops less rapidly, and there is still asymmetry about the maximum. As expected, without dispersion (i.e. in the 'top-hat' limit $K_d \to 0$ with no turbulent dispersion) the distribution of tracers $y_{F,a}/\left(F/{M_0}^{1/3}\right)$ has a discontinuity at η_a, the location of the advective front (defined in (3.24)), where it vanishes.

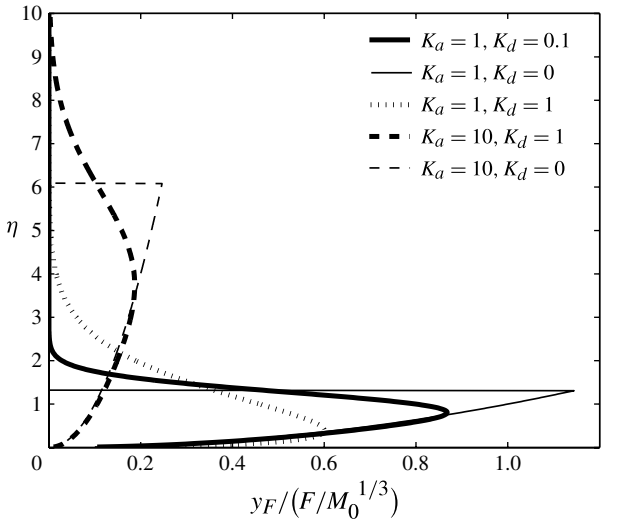

FIGURE 1. Plot of the variation of the non-dimensional similarity solution $y_F/\left(F/M_0{}^{1/3}\right)$, defined in (3.21), as a function of the similarity variable $\eta = z/\left(t^{2/3}M_0{}^{1/3}\right)$ for the problem of advection–dispersion in the case of a constant flux at the source and for different values of the advection and dispersion parameters, K_a and K_d, respectively. In the 'top-hat' limit $K_d \to 0$ with no turbulent dispersion, we use the non-dimensional similarity solution $y_{F,a}/\left(F/M_0{}^{1/3}\right)$ defined in (3.25).

We can observe in figure 1 that for the solution y_F of the general effective advection–diffusion problem a non-negligible portion of the volume of tracers is transported faster than the advective speed, due to the combined effects of advection and dispersion processes. We can compute the portion of the total volume of tracers β_F which travels ahead of the advective front via

$$\beta_F = \frac{\displaystyle\int_{\eta_a}^{\infty} y_F \,\mathrm{d}\eta}{\displaystyle\int_{0}^{\infty} y_F \,\mathrm{d}\eta}. \tag{3.26}$$

Using (3.21), we obtain

$$\beta_F = \frac{\Gamma\left[\dfrac{2}{3}\left(\dfrac{K_a}{K_d}+1\right), \dfrac{2K_a}{3K_d}\right] - \left(\dfrac{2K_a}{3K_d}\right)\Gamma\left[\dfrac{2}{3}\left(\dfrac{K_a}{K_d}-\dfrac{1}{2}\right), \dfrac{2K_a}{3K_d}\right]}{\Gamma\left[\dfrac{2}{3}\left(\dfrac{K_a}{K_d}+1\right)\right]}. \tag{3.27}$$

The ratio β_F remains constant in time and space because (3.27) does not depend on η. Moreover, β_F depends only on the ratio K_d/K_a. We have plotted β_F as a function of K_d/K_a in figure 2(*a*), in a log–log plot. We can prove that β_F tends asymptotically to 0 and indeed $\beta_F \sim O\left((K_d/K_a)^{1/2}\right)$ as $K_d/K_a \to 0$ (see equation (8.11.10) in NIST 2012), thus implying that the portion of tracers in the dispersive front becomes smaller as K_d/K_a increases (see figure 1 for the change in the distribution of y_F with various K_a and K_d). It appears that $\beta_F \approx 0.5\,(K_d/K_a)^{1/2}$ (plotted with a dashed curve) as $K_d/K_a \to 0$, but we could not establish the magnitude of the pre-multiplying factor

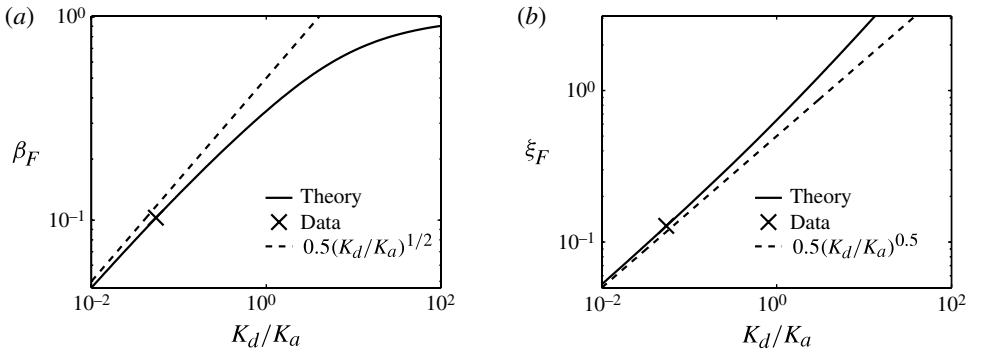

FIGURE 2. Constant-flux case for the tracer concentration. (*a*) A log–log plot of the theoretically predicted variation of β_F (defined in (3.27)), the portion of the total volume of tracers released which travels ahead of the advective front η_a (defined in (3.24)), as a function of K_d/K_a (plotted with a solid line), with the experimentally determined value (obtained from the best fit of the constant-flux case shown in figure 14) marked with a cross, and the asymptotic curve $0.5\,(K_d/K_a)^{1/2}$ plotted with a dashed line. (*b*) A log–log plot of the theoretically predicted variation of ξ_F (defined in (3.29)), the normalized distance between the average location of the volume of tracers travelling ahead of the advective front and the location of the advective front η_a, as a function of K_d/K_a (plotted with a solid line), with the experimentally determined value (obtained from the best fit of the constant-flux case shown in figure 14) marked with a cross, and the curve $0.5\,(K_d/K_a)^{0.5}$ plotted with a dashed line.

through asymptotic analysis. We can also compute the normalized distance between the average location of the volume of tracers travelling ahead of the advective front and the location of the advective front η_a,

$$\xi_F = \frac{1}{\eta_a}\left(\frac{\displaystyle\int_{\eta_a}^{\infty} y_F \eta \,\mathrm{d}\eta}{\displaystyle\int_{\eta_a}^{\infty} y_F \,\mathrm{d}\eta} - \eta_a\right), \tag{3.28}$$

which yields

$$\xi_F = \frac{3}{5}\left(\frac{3K_d}{2K_a}\right)^{2/3} \frac{\Gamma\left[\frac{2}{3}\left(\frac{K_a}{K_d}+2\right), \frac{2K_a}{3K_d}\right] - \left(\frac{2K_a}{3K_d}\right)^{5/3}\Gamma\left[\frac{2}{3}\left(\frac{K_a}{K_d}-\frac{1}{2}\right), \frac{2K_a}{3K_d}\right]}{\Gamma\left[\frac{2}{3}\left(\frac{K_a}{K_d}+1\right), \frac{2K_a}{3K_d}\right] - \left(\frac{2K_a}{3K_d}\right)\Gamma\left[\frac{2}{3}\left(\frac{K_a}{K_d}-\frac{1}{2}\right), \frac{2K_a}{3K_d}\right]} - 1. \tag{3.29}$$

We plot ξ_F as a function of K_d/K_a in figure 2(*b*), in a log–log plot. The distance ξ_F can be considered as the normalized distance between the dispersive front (average location of the particles travelling ahead of the advective front) and the advective front η_a (defined in (3.24)). In time and space coordinates, the distance between the dispersive front z_F and the advective front z_a is $z_F - z_a = \xi_F \eta_a t^{2/3}$. So the distance between the dispersive front and the advective front increases with time like $t^{2/3}$. We can also see in figure 2(*b*) that $\xi_F \to 0$ and it appears that $\xi_F \approx 0.5\,(K_d/K_a)^{0.5}$ (plotted with a dashed curve) as $K_d/K_a \to 0$, thus implying that the front becomes sharper as K_d/K_a decreases (see also figure 1).

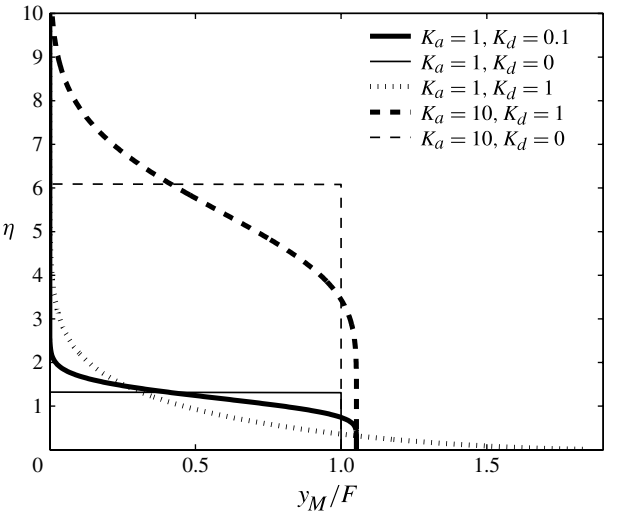

FIGURE 3. Plot of the variation of the normalized similarity solution y_M/F, defined in (3.30), as a function of the similarity variable $\eta = z/\left(t^{2/3}{M_0}^{1/3}\right)$ for the concentration flux of tracers in the case of a constant flux at the source F and for different values of the advection and dispersion parameters, K_a and K_d, respectively. In the 'top-hat' limit $K_d \to 0$ with no turbulent dispersion parametrized, we use the normalized piecewise-constant similarity solution $y_{M,a}/F$, defined in (3.31).

3.3. *Constant-flux release: concentration flux*

We can now study in space and time a somewhat more physically relevant quantity, i.e. the vertical (or streamwise) concentration flux of tracers $M_\phi = K_a {M_0}^{1/2}\phi/z^{1/2}$ defined in (2.5*b*). Thus, the solution of the concentration flux of tracers for the case of a constant source flux is, for $K_a > K_d/2$,

$$M_\phi(z,t) = y_M(\eta) = \frac{F}{1-\dfrac{K_d}{2K_a}}\,\frac{\Gamma\left[\dfrac{2}{3}\left(\dfrac{K_a}{K_d}-\dfrac{1}{2}\right),\dfrac{4\eta^{3/2}}{9K_d}\right]}{\Gamma\left[\dfrac{2}{3}\left(\dfrac{K_a}{K_d}-\dfrac{1}{2}\right)\right]} \quad \text{with } \eta = \frac{z}{t^{2/3}{M_0}^{1/3}}, \tag{3.30}$$

where we use the solution for the horizontally-integrated concentration $\phi = \phi_F = t^{1/3}y_F$, with y_F defined in (3.21). We can note that at the origin $\eta = 0$ the solution y_M depends on both F and a function of the ratio K_d/K_a.

For comparison with a purely advective flow, in the limit $K_d \to 0$ (relevant, as already noted, to 'top-hat' mean velocity profiles in the absence of parametrized streamwise turbulent dispersion) the concentration flux is

$$y_{M,a}(\eta) = \begin{cases} F, & 0 \leqslant \eta < \eta_a, \\ 0, & \eta_a < \eta, \end{cases} \tag{3.31}$$

according to $y_{F,a}$, defined in (3.25), and (2.5*b*) with $\phi = \phi_{F,a} = t^{1/3}y_{F,a}$.

We have plotted the normalized tracer flux y_M/F, as well as $y_{M,a}/F$, as functions of the similarity variable $\eta = z/\left(t^{2/3}{M_0}^{1/3}\right)$ in figure 3. The five different curves show the concentration profile in similarity form for different values of K_a and K_d. As we increase the advection parameter the flux of tracers extends from the origin

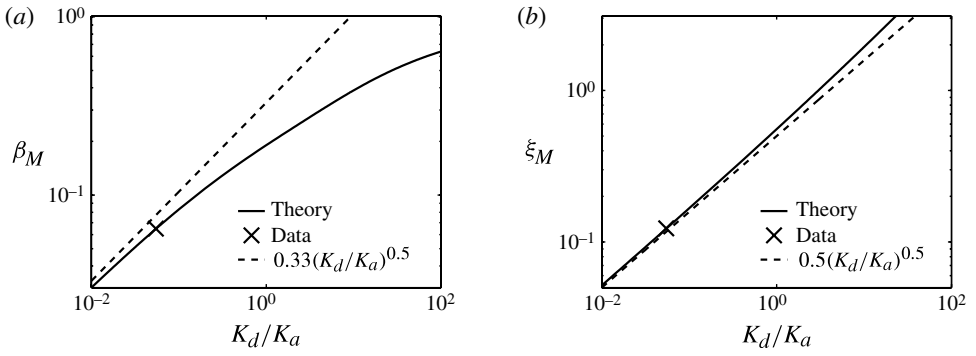

FIGURE 4. Constant-flux case for the tracer flux. (*a*) A log–log plot of the theoretically predicted variation of β_M (defined in (3.33)), the portion of the total concentration flux of tracers ahead of the advective front η_a (defined in (3.24)), as a function of K_d/K_a (plotted with a solid line), with the experimentally determined value (obtained from the best fit of the constant-flux case shown in figure 14) marked with a cross, and the curve $0.33\,(K_d/K_a)^{0.5}$ plotted with a dashed line. (*b*) A log–log plot of the theoretically predicted variation of ξ_M (defined in (3.35)), the normalized distance between the average location of the concentration flux of tracers ahead of the advective front and the location of the advective front η_a, as a function of K_d/K_a (plotted with a solid line), with the experimentally determined value (obtained from the best fit of the constant-flux case shown in figure 14) marked with a cross, and the curve $0.5\,(K_d/K_a)^{0.5}$ plotted with a dashed line.

into a plateau before dropping smoothly at the front and eventually vanishing at large η. In the purely advective case (i.e. in the 'top-hat' limit $K_d \to 0$ with no turbulent dispersion), the solution $y_{M,a}/F$ has a discontinuity at the location of the advective front η_a (defined in (3.24)). The steepness of the front tends to decrease with increasing dispersion parameter. Moreover, we can see that the value at the origin $y_M(\eta = 0)/F$ decreases with decreasing K_d/K_a, from $y_M(0)/F \to \infty$ as $K_d/K_a \to \infty$ to $y_M(0)/F \to 1$ as $K_d/K_a \to 0$.

In a similar fashion to the previous subsection (cf. (3.26) and (3.28)), we can compute the portion of the total concentration flux of tracers β_M which is ahead of the advective front η_a via

$$\beta_M = \frac{\displaystyle\int_{\eta_a}^{\infty} y_M \,\mathrm{d}\eta}{\displaystyle\int_0^{\infty} y_M \,\mathrm{d}\eta}. \tag{3.32}$$

Using (3.30), we obtain

$$\beta_M = \frac{\Gamma\left[\dfrac{2}{3}\left(\dfrac{K_a}{K_d}+\dfrac{1}{2}\right), \dfrac{2K_a}{3K_d}\right] - \left(\dfrac{2K_a}{3K_d}\right)^{2/3} \Gamma\left[\dfrac{2}{3}\left(\dfrac{K_a}{K_d}-\dfrac{1}{2}\right), \dfrac{2K_a}{3K_d}\right]}{\Gamma\left[\dfrac{2}{3}\left(\dfrac{K_a}{K_d}+\dfrac{1}{2}\right)\right]}. \tag{3.33}$$

As before, the ratio β_M remains constant in time and space because (3.33) does not depend on η; and β_M depends only on the ratio K_d/K_a. We have plotted β_M as a function of K_d/K_a in figure 4(*a*), in a log–log plot. Similarly to β_F, it appears that $\beta_M \to 0$ and $\beta_M \approx 0.33\,(K_d/K_a)^{0.5}$ (plotted with a dashed curve) as $K_d/K_a \to 0$, thus

implying that the portion of the tracer flux in the dispersive front becomes smaller as K_d/K_a decreases. Figure 3 shows the change in the distribution of y_M with various K_a and K_d. We can also compute the normalized distance between the average location of the tracer flux ahead of the advective front and the location of the advective front η_a,

$$\xi_M = \frac{1}{\eta_a}\left(\frac{\displaystyle\int_{\eta_a}^{\infty} y_M \eta \,\mathrm{d}\eta}{\displaystyle\int_{\eta_a}^{\infty} y_M \,\mathrm{d}\eta} - \eta_a\right), \tag{3.34}$$

which yields

$$\xi_M = \frac{1}{2}\left(\frac{3K_d}{2K_a}\right)^{2/3} \frac{\Gamma\left[\frac{2}{3}\left(\frac{K_a}{K_d}+\frac{3}{2}\right), \frac{2K_a}{3K_d}\right] - \left(\frac{2K_a}{3K_d}\right)^{4/3}\Gamma\left[\frac{2}{3}\left(\frac{K_a}{K_d}-\frac{1}{2}\right), \frac{2K_a}{3K_d}\right]}{\Gamma\left[\frac{2}{3}\left(\frac{K_a}{K_d}+\frac{1}{2}\right), \frac{2K_a}{3K_d}\right] - \left(\frac{2K_a}{3K_d}\right)^{2/3}\Gamma\left[\frac{2}{3}\left(\frac{K_a}{K_d}-\frac{1}{2}\right), \frac{2K_a}{3K_d}\right]} - 1. \tag{3.35}$$

We plot ξ_M in figure 4(*b*), in a log–log plot. Similarly to ξ_F (see figure 2*b*), we can also see in figure 4(*b*) that $\xi_M \to 0$ and $\xi_M \approx 0.5\,(K_d/K_a)^{0.5}$ (plotted with a dashed curve) as $K_d/K_a \to 0$, thus implying that the front becomes sharper as K_d/K_a decreases.

3.4. *Finite-volume release: instantaneous release fundamental solution*

We can also consider an instantaneous finite-volume release localized at the source of a quasi-two-dimensional steady turbulent jet. If the general (2.5) is satisfied for $z > 0$, $t > 0$ and if, in addition, $\phi(z, t)$ satisfies (following (3.1*a–c*) with $\vartheta = 0$)

$$\phi(z,0) = B\delta(z), \quad \phi(z,t) \to 0 \quad \text{as } z \to \infty, \quad \int_0^{\infty} \phi(z,t)\,\mathrm{d}z = B \quad \text{for } t > 0, \tag{3.36a–c}$$

where B is a constant representing the total volume of tracers released and $\delta(z)$ is a Dirac delta function, then the condition (3.36*c*) can hold for all $t > 0$ if and only if $c = -a$ according to (3.7) with $\vartheta = 0$. Thus, (3.4) becomes

$$\phi(z,t) = t^{-2/3} y(\eta) \quad \text{with } \eta = \frac{z}{t^{2/3} {M_0}^{1/3}}. \tag{3.37}$$

In this case, the initial boundary value problem for $\phi(z, t)$, defined by (3.5) with $c = -a$, (3.36*a–c*) and (3.37), reduces to

$$\left(-\frac{2}{3} - \frac{K_a}{2\eta^{3/2}}\right) y + \left(\frac{(2K_a - K_d)}{2\eta^{1/2}} - \frac{2\eta}{3}\right) y' - K_d \eta^{1/2} y'' = 0, \tag{3.38}$$

subject to the conditions

$$y(\eta) \to 0 \quad \text{as } \eta \to \infty, \quad \int_0^{\infty} y(\eta)\,\mathrm{d}\eta = \frac{B}{{M_0}^{1/3}} \quad \text{for } t > 0. \tag{3.39a,b}$$

Equation (3.38) can be rearranged as

$$-\frac{2}{3}(\eta y)' + K_a\left(\frac{y}{\eta^{1/2}}\right)' - K_d\left(\eta^{1/2} y'\right)' = 0, \tag{3.40}$$

and thus integrated twice to obtain

$$y(\eta) = \eta^{K_a/K_d} \exp\left[-\frac{4}{9K_d}\eta^{3/2}\right] \times \left(J_4 + \frac{2J_3}{3}\left(-\frac{4}{9K_d}\right)^{2/3\left(K_a/K_d-1\right)} \gamma\left[\frac{2}{3}\left(1-\frac{K_a}{K_d}\right), -\frac{4}{9K_d}\eta^{3/2}\right]\right), \quad (3.41)$$

where J_3 and J_4 are two integration constants and, once again, $\gamma[g,\zeta] = \int_0^\zeta h^{g-1}\mathrm{e}^{-h}\,\mathrm{d}h$ is the lower incomplete gamma function. Since $\eta > 0$ and the function $\gamma[g,\zeta]$ is complex for $\zeta < 0$, J_3 must equal zero. J_4 can be determined by integrating (3.41),

$$\int_0^\infty y(\eta)\,\mathrm{d}\eta = J_4\left(\frac{3}{2}\right)^{4/3(K_a/K_d+1/4)} {K_d}^{2/3(K_a/K_d+1)}\Gamma\left[\frac{2}{3}\left(\frac{K_a}{K_d}+1\right)\right], \quad (3.42)$$

and applying the integral condition (3.39*b*) to obtain

$$J_4 = \frac{B}{\left(\frac{3}{2}\right)^{4/3(K_a/K_d+1/4)} {K_d}^{2/3(K_a/K_d+1)}\Gamma\left[\frac{2}{3}\left(\frac{K_a}{K_d}+1\right)\right] {M_0}^{1/3}}. \quad (3.43)$$

Therefore, the 'fundamental' solution of the effective advection–diffusion problem for the case of an instantaneous finite-volume release initially localized as a delta function at $z = 0$ is

$$y_\delta(\eta) = \frac{B}{\left(\frac{3}{2}\right)^{4/3(K_a/K_d+1/4)} {K_d}^{2/3(K_a/K_d+1)}\Gamma\left[\frac{2}{3}\left(\frac{K_a}{K_d}+1\right)\right] {M_0}^{1/3}} \eta^{K_a/K_d} \times \exp\left[-\frac{4}{9K_d}\eta^{3/2}\right]. \quad (3.44)$$

We have plotted the non-dimensional quantity $y_\delta/\left(B/{M_0}^{1/3}\right)$ as a function of the similarity variable $\eta = z/\left(t^{2/3}{M_0}^{1/3}\right)$ in figure 5. The three different curves show the concentration profile in similarity form for different values of K_a and K_d. Unsurprisingly, we find that the location of the peak, $\eta_{max} = (3K_a/2)^{2/3}$, only depends on K_a. Increasing K_a shifts the peak upwards away from the origin, while increasing K_d spreads the width of the distribution. There is always to a greater or lesser extent asymmetry, with the leading edge being more diffuse than the rear.

Interestingly, in the 'top-hat', purely advective limit $K_d \to 0$ with no turbulent dispersion equation (3.40) integrates to

$$\left(\frac{K_a}{\eta^{1/2}} - \frac{2\eta}{3}\right) y = J_5, \quad (3.45)$$

where J_5 is a constant of integration. In order to satisfy the boundary condition at infinity (3.39*a*) as well as the integral condition (3.39*b*), $J_5 = 0$ for all $0 \leqslant \eta < \eta_a$ and $\eta_a < \eta$, where $\eta_a = (3K_a/2)^{2/3}$ is the location of the advective front as defined in (3.24). We can note that the formula of η_a is the same in both the constant-flux case and the finite-volume case. Therefore, the similarity solution of the purely advective problem for the case of an instantaneous finite-volume release initially localized as a delta function at $z = 0$ is

$$y_{\delta,a} = B\delta(\eta - \eta_a). \quad (3.46)$$

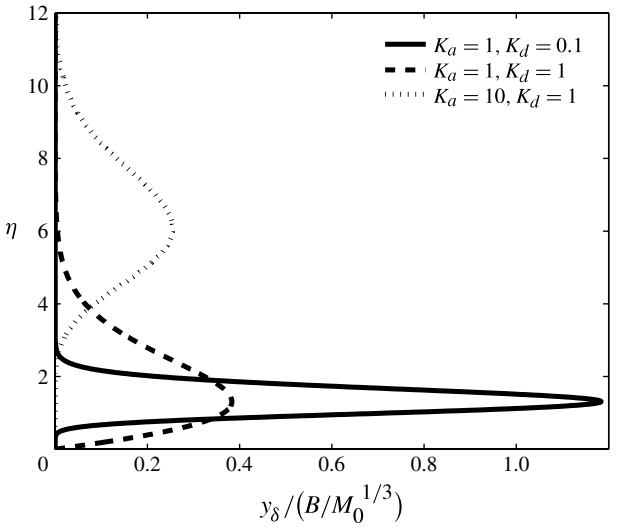

FIGURE 5. Plot of the variation of the non-dimensional fundamental similarity solution $y_\delta/\left(B/M_0^{1/3}\right)$, defined in (3.44), as a function of the similarity variable $\eta = z/\left(t^{2/3}M_0^{1/3}\right)$ for the problem of advection–dispersion in the case of an instantaneous finite-volume release at the source and for different values of the advection and dispersion parameters, K_a and K_d, respectively.

As expected, without dispersion the initial Dirac delta distribution of tracers persists for all time. The delta function is located in the similarity domain at $\eta_a = (3K_a/2)^{2/3}$, the location of the (purely) advective front. In time and space coordinates, this means that the volume of tracers is located at $z_a = (3K_a/2)^{2/3}\, t^{2/3}$ and travels at the speed $w_a = K_a M_0^{1/2} z^{-1/2}$ in the streamwise direction. We can notice that the location of the advective front η_a is the same as the location of the peak of the tracer concentration in the general effective advection–diffusion problem: $\eta_a = \eta_{max} = (3K_a/2)^{2/3}$. Consequently, and similarly to the constant-flux case, in the general effective advection–diffusion problem a non-negligible portion of the volume of tracers is transported faster than the advective speed due to the combined effects of advection and dispersion processes. We can compute the portion of the total volume of tracers β_B which travels ahead of the advective front via

$$\beta_B = \frac{\displaystyle\int_{\eta_a}^{\infty} y_\delta \,\mathrm{d}\eta}{\displaystyle\int_0^{\infty} y_\delta \,\mathrm{d}\eta}. \tag{3.47}$$

Using (3.44), we obtain

$$\beta_B = \frac{\Gamma\left[\dfrac{2}{3}\left(\dfrac{K_a}{K_d}+1\right), \dfrac{2K_a}{3K_d}\right]}{\Gamma\left[\dfrac{2}{3}\left(\dfrac{K_a}{K_d}+1\right)\right]}, \tag{3.48}$$

where, once again, $\Gamma[g,\zeta] = \int_\zeta^\infty h^{g-1}\mathrm{e}^{-h}\,\mathrm{d}h$ is the upper incomplete gamma function. As in the constant-flux release case β_F defined in (3.27), the ratio β_B remains constant

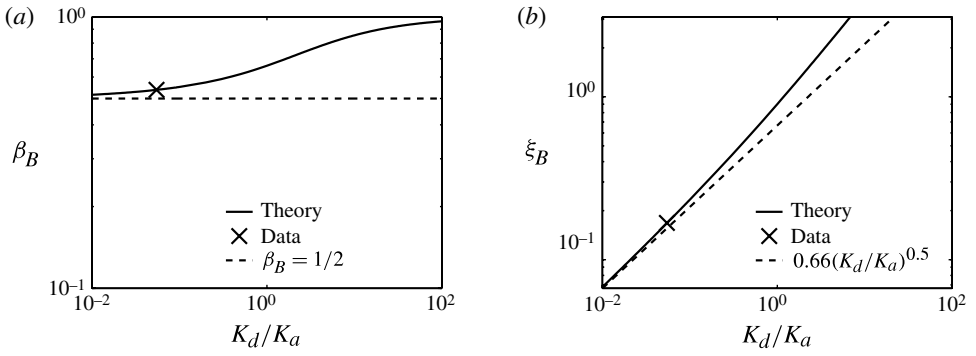

FIGURE 6. Finite-volume case for an instantaneous release. (*a*) A plot of the theoretically predicted variation of β_B (defined in (3.48)), the portion of the total volume of tracers released which travels ahead of the advective front η_a (defined in (3.24)), as a function of K_d/K_a (plotted with a solid line), with the experimentally determined value (obtained from the best fit of the constant-flux case shown in figure 14) marked with a cross, and the asymptotic value $\beta_B = 0.5$ plotted with a dashed line. (*b*) A log–log plot of the theoretically predicted variation of ξ_B (defined in (3.50)), the normalized distance between the average location of the volume of tracers travelling ahead of the advective front and the location of the advective front η_a, as a function of K_d/K_a (plotted with a solid line), with the experimentally determined value (obtained from the best fit of the constant-flux case shown in figure 14) marked with a cross, and the curve $0.66\,(K_d/K_a)^{0.5}$ plotted with a dashed line.

in time and space because (3.48) does not depend on η. Moreover, β_B depends only on the ratio K_d/K_a. We have plotted β_B as a function of K_d/K_a in figure 6(*a*). However, in contrast to β_F, we can prove that $\beta_B \to 1/2$ (plotted with a dashed line) as $K_d/K_a \to 0$ (see equation (8.11.10) in NIST 2012), thus implying that the distribution of tracers y_δ becomes more symmetrical with respect to the peak value as K_d/K_a decreases. Figure 5 shows the change in the distribution of y_δ with various K_a and K_d. We can also compute the normalized distance between the average location of the volume of tracers travelling ahead of the advective front and the location of the advective front η_a,

$$\xi_B = \frac{1}{\eta_a}\left(\frac{\displaystyle\int_{\eta_a}^{\infty} y_\delta \eta \,\mathrm{d}\eta}{\displaystyle\int_{\eta_a}^{\infty} y_\delta \,\mathrm{d}\eta} - \eta_a\right), \tag{3.49}$$

which yields

$$\xi_B = \left(\frac{3K_d}{2K_a}\right)^{2/3} \frac{\Gamma\left[\dfrac{2}{3}\left(\dfrac{K_a}{K_d}+2\right), \dfrac{2K_a}{3K_d}\right]}{\Gamma\left[\dfrac{2}{3}\left(\dfrac{K_a}{K_d}+1\right), \dfrac{2K_a}{3K_d}\right]} - 1. \tag{3.50}$$

We plot ξ_B in figure 6(*b*), in a log–log plot. Similarly to the constant-flux case ξ_F defined in (3.29), the normalized distance ξ_B can also be considered as the distance between the dispersive front, i.e. the average location of the particles travelling ahead of the advective front, and the advective front η_a. In time and space coordinates, the distance between the dispersive front z_B and the advective front z_a is $z_B - z_a = \xi_B \eta_a t^{2/3}$.

This distance increases with time as $t^{2/3}$, as we observed in the constant-flux case. We can also see in figure 6(*b*) that $\xi_B \to 0$, and it appears that $\xi_B \approx 0.66\,(K_d/K_a)^{0.5}$ (plotted with a dashed curve) as $K_d/K_a \to 0$, thus implying that the spreading of the tracer distribution becomes small compared with the distance between the peak and the origin as K_d/K_a decreases (see also figure 5).

3.5. *Finite-volume release: time-dependent release general solution*

The solution $\phi_\delta(z,t) = t^{-2/3} y_\delta(\eta)$ is the response of the system described by the effective advection–diffusion equation (2.5) to a finite volume released instantaneously at $t = 0$ and distributed spatially according to a Dirac delta function $\delta(z)$. Due to the linearity of (2.5), we can construct from this 'fundamental' solution ϕ_δ an integral expression for the general solution ϕ_g for a finite volume B being released at the origin $z = 0$ over a period of time such that $\phi_g(0,t) = f(t)$. Without loss of generality, we choose to normalize the source function $f(t)$:

$$\int_{-\infty}^{\infty} f(t)\,\mathrm{d}t = 1. \tag{3.51}$$

Therefore, the general solution ϕ_g can be expressed as the following integral:

$$\phi_g(z,t) = \int_0^t (t-\tau)^{-2/3}\, y_\delta(\eta_\tau) f(\tau)\,\mathrm{d}\tau \quad \text{with } \eta_\tau = \frac{z}{(t-\tau)^{2/3} {M_0}^{1/3}}. \tag{3.52}$$

The case of a truly instantaneous release of a finite volume at $(z,t) = (0,0)$ is physically impossible to realize in an experiment. It is also not ideal in the modelling of real flows. A more realistic set of initial boundary conditions is to have a finite volume released at a constant flux over a finite period of time $0 \leqslant t \leqslant T_0$. This problem can be defined in terms of the following conditions:

$$\phi_{T_0}(z,t) \to 0 \quad \text{as } z \to \infty, \qquad \int_0^\infty \phi_{T_0}(z,t)\,\mathrm{d}z = \begin{cases} \dfrac{Bt}{T_0}, & 0 \leqslant t \leqslant T_0, \\ B, & T_0 < t, \end{cases} \tag{3.53a,b}$$

with ϕ_{T_0} satisfying the general (2.5) for $z > 0$, $t > 0$. The solution to this initial boundary value problem can be computed using (3.52) with the source function

$$f_{T_0}(t) = \frac{H(t) - H(t-T_0)}{T_0}, \tag{3.54}$$

where H is the Heaviside function (i.e. $H(t) = 0$ for all $t < 0$ and $H(t) = 1$ for all $t > 0$). We find that the solution to the integral (3.52) with the source function f_{T_0} described by (3.54) is

$$\phi_{T_0}(z,t) = \frac{2Bz^{1/2}}{3K_d {M_0}^{1/2} T_0 \Gamma\left[\dfrac{2}{3}\left(\dfrac{K_a}{K_d}+1\right)\right]} \left(\Gamma\left[\frac{2}{3}\left(\frac{K_a}{K_d}-\frac{1}{2}\right), \frac{4z^{3/2}}{9K_d {M_0}^{1/2} t}\right] - \begin{cases} 0, & 0 < t \leqslant T_0, \\ \Gamma\left[\dfrac{2}{3}\left(\dfrac{K_a}{K_d}-\dfrac{1}{2}\right), \dfrac{4z^{3/2}}{9K_d {M_0}^{1/2}(t-T_0)}\right], & T_0 < t. \end{cases} \right) \tag{3.55}$$

The upper incomplete gamma function, $\Gamma[g,\zeta] = \int_\zeta^\infty h^{g-1} \mathrm{e}^{-h}\,\mathrm{d}h$, requires $g > 0$, hence this solution is well-defined only for $K_a > K_d/2$. As we mentioned previously, we will

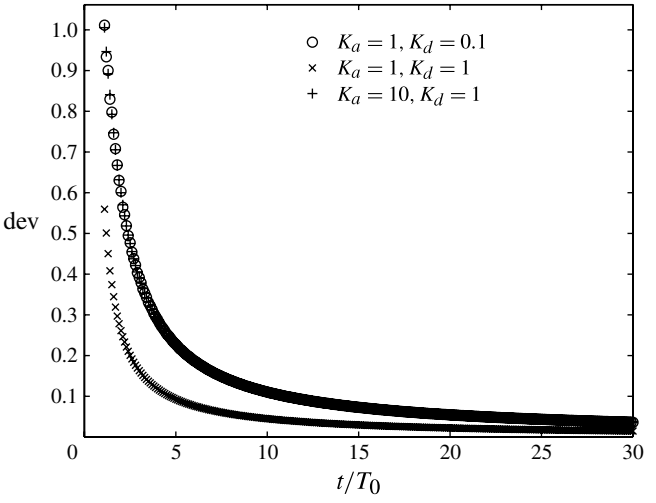

FIGURE 7. Variation with scaled time $\breve{t} = t/T_0$ of the normalized absolute deviation dev($\breve{t}$), defined in (3.58), of the general solution $\phi_{T_0}(z, t)$, defined in (3.55), and the fundamental solution $\phi_\delta(z, t)$ (defined by (3.44) and (3.37)). The data are computed numerically for different values of the advection and dispersion parameters.

find later that for our experimental data K_a appears to be substantially greater than K_d. Note that this solution cannot be written in similarity form because of the dependence on the time constant T_0.

We can prove (see the Appendix) that the solution $\phi_{T_0}(z, t)$, described in (3.55), satisfies

$$\phi_{T_0}(z, t) = \phi_\delta(z, t) \quad \text{for } \frac{t}{T_0} \gg 1. \tag{3.56}$$

So, the general solution for a rectangular source function converges asymptotically to the fundamental solution $\phi_\delta(z, t)$(defined by (3.44) and (3.37)) in the limit $t \gg T_0$. It is interesting to study how fast ϕ_{T_0} converges towards ϕ_δ. We can define the dimensionless distance $\breve{z}$ and the dimensionless time $\breve{t}$ using the scalings for length and time scales ${T_0}^{2/3}{M_0}^{1/3}$ and T_0, respectively, such as

$$\breve{z} = \frac{z}{{T_0}^{2/3}{M_0}^{1/3}}, \quad \breve{t} = \frac{t}{T_0}, \tag{3.57a,b}$$

where breves denote non-dimensional variables. The evolution in time of the normalized absolute deviation of the general solution ϕ_{T_0} from the fundamental solution ϕ_δ is

$$\mathrm{dev}(\breve{t}) = \frac{\displaystyle\int_0^\infty |\phi_{T_0}(\breve{z}, \breve{t}) - \phi_\delta(\breve{z}, \breve{t})| \, \mathrm{d}\breve{z}}{\displaystyle\int_0^\infty \phi_\delta(\breve{z}, \breve{t}) \, \mathrm{d}\breve{z}} \quad \text{for } \frac{t}{T_0} \geqslant 1, \tag{3.58}$$

a non-dimensional quantity which only depends on the advection and dispersion parameter K_a and K_d, and in particular does not depend on the total injected volume of tracers B, on the initial momentum M_0 or on the period of injection T_0. We plot dev($\breve{t}$) in figure 7 for $1 \leqslant t/T_0 \leqslant 30$. We compute the deviation numerically for

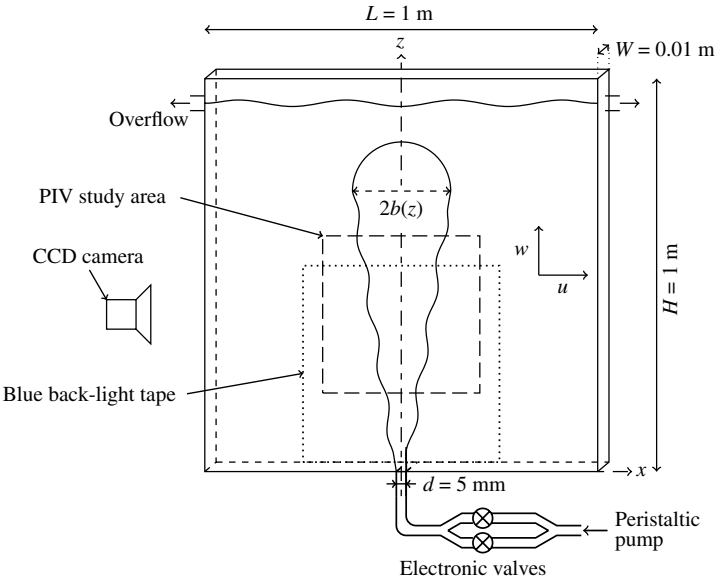

FIGURE 8. Schematic diagram of the experimental apparatus.

three different sets of values of K_a and K_d. We can see that all the curves decrease asymptotically towards zero as t/T_0 increases. The deviation is smaller than 0.1, which can be considered as a threshold value of near convergence, for $t/T_0 > 11$, $t/T_0 > 4.7$ and $t/T_0 > 11$ for the sets of advection and dispersion parameters $(K_a = 1, K_d = 0.1)$, $(K_a = 1, K_d = 1)$ and $(K_a = 10, K_d = 1)$, respectively. It appears that the deviation depends mainly but not entirely on the ratio K_d/K_a.

Furthermore, we can note that in (3.55), if we take the limit $T_0 \to \infty$ and define $F = B/T_0$, then we find

$$\phi_{T_0 \to \infty}(z, t) = t^{1/3} y_F(\eta), \tag{3.59}$$

with $\eta = z/\left(t^{2/3} {M_0}^{1/3}\right)$ consistently with (3.9). So, the solution for the constant-flux case described in (3.21) is equivalent to the asymptotic solution of the general solution ϕ_{T_0} if the period of release T_0 extends to infinity.

4. Experimental procedure

We conduct our experiments in a slight modification of the experimental apparatus we used in Landel *et al.* (2012), as shown schematically in figure 8. We conduct three distinct sets of experiments using two qualitatively different techniques. Each set of experiments is designed to provide experimental data that can be compared with the three theoretical predictions derived in the previous section for a constant-flux release, an instantaneous finite-volume release, and a non-instantaneous finite-volume release. In the first set of experiments, we measure the distribution of the concentration of dye as it is released at a constant flux at the source of quasi-two-dimensional steady turbulent jets. The second set of experiments involves what we believe to be a new technique, which consists of tracking large quantities of virtual particles evolving as passive tracers in the velocity field of quasi-two-dimensional steady turbulent jets. The velocity field is measured in experiments with real jets (as opposed to numerically

computed jets) by using particle image velocimetry (PIV). We designed this technique, which we designate as virtual particle tracking, to obtain data for an instantaneous release to compare with our mathematical model. We also consider virtual particle tracking to be complementary to experiments tracking the dispersion of the 'real' dye tracer. In the third set of experiments, we measure the distribution of the concentration of dye following the release of finite volumes of dye at the source into quasi-two-dimensional steady turbulent jets. For physical reasons, which will be detailed below, we cannot release finite volumes of dye instantaneously in the jets, and so such physical dye releases inevitably extended over a finite time interval.

For all the experiments, the jet Reynolds number at the source is approximately within the range $2100 \leqslant Re_j = dw_s/\nu \leqslant 4000$, where w_s is the source velocity and ν is the kinematic viscosity of water. In the jet, the Reynolds number (defined as $Re = b\overline{w}_m/\nu$) increases with streamwise distance from the source like $z^{1/2}$. We find that in the region where the jet can be considered quasi-two-dimensional (i.e. for $z/d \geqslant 20$), the Reynolds number is greater than 5000. Therefore, we believe that the flow is fully turbulent in the area of study.

4.1. *Constant-flux releases of dye*

We fill the 1 m(L) $\times$ 0.01 m(W) $\times$ 1 m(H) tank displayed in figure 8 with fresh tap water. A vertical jet of constant source volume flow rate is discharged into the tank using a peristaltic pump (520DU/R2 Watson–Marlow variable speed pump) fed by a constant-head tank.

The injection mechanism for the constant-flux releases of dye in steady turbulent quasi-two-dimensional jets consists of a syringe-pump connected to a small needle inserted into a single main tube. The needle is located 0.2 m upstream of the nozzle. After the jet has reached a steady state in the tank, a mixture of red food dye 'Fiesta Red' (Allura Red AC, E129) and tap water (with a dye concentration of 1.8 % per weight) is injected at a constant flow rate, 0.11 cm^3 s^{-1}. We study 19 constant-flux releases of dye in steady turbulent jets with jet Reynolds number $2240 \leqslant Re_j = dw_s/\nu \leqslant 3870$.

To measure the dye concentration, we perform the experiments in a dark room. Following Dalziel *et al.* (2008), we attach a 0.54 m $\times$ 0.54 m electroluminescent Light Tape (Electro-LuminX Lighting Corporation) to the external surface of the rear side of the tank, centred on the jet axis and with the bottom of the tape at the height of the nozzle. It provides a constant and uniform source of near-monochromatic cyan light of approximately 400 cd m^{-2}. This wavelength is close to the peak of the 'Fiesta Red' dye absorption spectrum. We measure the transmitted light intensity with a high-speed 8 bit grey-scale camera (Fastcam SA1.1 – Photron) mounted with an 85 mm focal-length lens (f-stop 5.6). The camera is located 3 m away from the tank, which is sufficient to have negligible parallax error. We also take care to reduce any light pollution from reflection or other sources, in particular by installing a black frame around the study area. The camera records 640 $\times$ 848 pixel images covering the entire study area, which spans $-40 \leqslant x/d \leqslant 40$ and $0 \leqslant z/d \leqslant 100$ (where x is the coordinate in the lateral, cross-jet or horizontal direction, and z is the coordinate in the streamwise or vertical direction; the origin is at the centre of the nozzle slot and $d = 5$ mm is the nozzle width), and part of the black frame (in order to have a black intensity reference). For each video we set the origin in time, $t = 0$, at the image preceding the first image in which dye is seen by the camera. The frequency of image acquisition is set at 60 Hz. Following the calibration method and the algorithm described by Coomaraswamy (2011) and based on Cenedese &

Dalziel (1998), we perform the calibration *in situ*. We record the intensity measured by the camera for 23 known concentrations of dye, ranging from 0 to 2 % per weight. A fitting curve using a third-order polynomial in the logarithm of the normalized intensity gives us a continuous and monotonic relationship between the intensity and the concentration. All the images recorded by the camera, either for the calibration process or for the experiments, are analysed using the software code DigiFlow (Sveen & Dalziel 2005). This procedure enables us to obtain accurate measurements of the (spanwise-integrated) dye concentration in time and space for each experiment.

4.2. *Instantaneous finite-volume releases of virtual particles*

We track virtual particles in experimentally measured velocity fields of quasi-two-dimensional steady turbulent jets. We use the velocity fields measured by us previously as reported in Landel *et al.* (2012) and obtained using a PIV technique (as described in Sveen & Dalziel 2005). We measure the jet velocity in a 0.4 m × 0.4 m study area centred on the jet axis (as shown in figure 8) and covering a height from $z = 0.2$ m to 0.6 m. We use the camera described above (mounted with a 62 mm focal-length lens) at a frequency of image acquisition 250 Hz and for a duration of 21.8 s. The 1024 × 1024 pixel images provide us with spatially and temporally resolved velocity fields for six steady turbulent jets at source volume flow rates 33.2, 37.0 and 40.3 $\mathrm{cm}^3\ \mathrm{s}^{-1}$. The jet Reynolds number is in the range $3320 \leqslant Re_j \leqslant 4030$. We find that the divergence of each velocity field is insignificant (typically $\mathrm{mean}(|\boldsymbol{\nabla}\cdot\boldsymbol{u}|)/\mathrm{mean}(|\boldsymbol{\nabla}\times\boldsymbol{u}|) \approx 5\,\%$, where mean(·) represents an average in time and space), so they can be considered as incompressible. Using these computed velocity fields, we seed in each of them 201 × 51 pixel clusters of (massless) virtual particles located in a rectangular evenly-distributed cluster at $-8.8 \leqslant x/d \leqslant 7$ and $44.4 \leqslant z/d \leqslant 48.3$ (i.e. within the characteristic local width of the jet). The release can be considered instantaneous as a cluster of virtual particles is injected in the flow field within a single time step. The possibility of releasing instantaneously a large number of particles constitutes the main reason for the use of this technique in this study. This important advantage, compared with the non-instantaneous dye finite-volume releases (discussed below), allows us to reproduce more easily the instantaneous release constraint imposed in the mathematical model in (3.36*a*).

We release individual clusters every 0.4 s in each experiment and study a total of 256 clusters representing 2 624 256 virtual particles. For each cluster the virtual particles evolve in time and space as passive tracers advected by the flow. For each simulation we set the origin in time, $t = 0$, at the first image in which the particle cluster is seeded. The simulation of a cluster stops as soon as a virtual particle reaches the top boundary of the velocity field. Finally, we record the location in time and space of the tracers and analyse the results using DigiFlow. By averaging 256 virtual particle experiments we obtain a smooth distribution of the particle concentration in time and space, which we compare with the dye experiments and the theoretical prediction in § 5.

Different techniques involving particle tracking have been used to study dispersion, mixing and transport in jets or other types of flows. In previous studies, the particles were either real and tracked by an imaging analysis technique (see e.g. Yang *et al.* 2000; Sveen & Dalziel 2005), or purely numerical and evolving in numerically resolved flows (see e.g. Dutkiewicz, Griffa & Olson 1993; Luo *et al.* 2006; Picano *et al.* 2010). However, we have not been able to find any mention in the literature of using virtual particles in the velocity field of real flows. This technique requires

a spatially and temporally resolved computation of the velocity field, which can be done, for example, using a PIV technique. We can then seed some (massless) virtual particles in the velocity field and track their trajectory as they are advected as passive tracers by the flow. The advantages of this complementary technique are numerous: the resolution is only limited by the resolution of the acquisition of the velocity field; it is not restricted to the computation limitations encountered in full numerical simulations, but can be used for any laboratory experiment; a large quantity of virtual particles can be seeded instantaneously in the jet (thus satisfying, in our case, the constraint imposed in the theoretical model for an instantaneous finite-volume release); and their initial distribution can be completely arbitrary.

4.3. *Finite-volume releases of dye*

The experimental procedure for the finite-volume releases of dye in steady turbulent quasi-two-dimensional jets is very similar to the experimental procedure for the constant-flux releases of dye (described in § 4.1). We fill the tank displayed in figure 8 with fresh tap water. A vertical jet of constant source volume flow rate is discharged into the tank using the same peristaltic pump described above and fed by a constant-head tank.

For the injection mechanism of the finite-volume releases of dye, the main tube divides into two approximately 80 cm before the nozzle (see figure 8). The two tubes are recombined approximately 15 cm before the nozzle. Two valves located just before the recombining junction control the flow for each pipe separately. We monitor the valves to allow the flow to go through one section or the other exclusively. We open and close the valves electronically so that a steady jet flow is maintained in the tank before and after switching the valves. Although we observe a small perturbation (a pressure wave) in the tank we believe it does not perturb the experiment significantly. The purpose of this two-tube system is to release a finite volume of dye in a steady turbulent jet. The procedure for each experiment is as follows. We inject a 5 cm^3 mixture of the same red food dye described above and tap water (with a dye concentration of 2 % per weight) into the closed tube approximately 5 mm upstream of the valve. Meanwhile, water flows at a constant source volume flow rate through the other tube to produce a turbulent jet in the tank. After the jet reaches a steady state, we switch the valves to redirect the whole flow into the section containing the red dye, thus releasing a finite volume of dye into the established jet. We conduct 26 finite-volume releases of dye in steady turbulent jets with jet Reynolds number $2170 \leqslant Re_j \leqslant 4870$. It is important to note that, although great care is taken during the experiments and different protocols have been tested, instantaneous finite-volume releases of dye cannot be achieved for practical reasons. We find that the time of injection, although relatively short (of the order of 0.5 s), cannot be considered as instantaneous, as we will discuss in § 5.4. We believe that the main reason for this injection delay is some laminar Taylor dispersion (Taylor 1953) of the dye as it is transported in the short section of tube (approximately 0.2 m long) leading to the tank.

We perform the measurements of the dye concentration for the finite-volume releases using exactly the same technique as described for the constant-flux releases. From the transmitted light intensity recorded by the high-speed camera described above, we can compute the dye concentration in the study area, spanning $-40 \leqslant x/d \leqslant 40$ and $0 \leqslant z/d \leqslant 100$, at a frequency of 60 Hz. We obtain accurate measurements of the dye concentration in time and space for each experiment.

5. Experimental results

Similarly to Landel *et al.* (2012), we find that the natural scalings for length and time in our problem are d, the source width, and (d^2/Q_0), respectively. Therefore, when considering our experimental data we will always scale quantities with these scalings, i.e.

$$z = d\tilde{z}, \quad t = \left(\frac{d^2}{Q_0}\right)\tilde{t}, \tag{5.1a,b}$$

where tildes denote non-dimensional variables. Although the initial momentum flux M_0 is also a natural scaling parameter in the theoretical model (see (2.4*b*), (2.5) and (3.4)), we do not use it as a scaling parameter in this section because we could not measure it directly in the experiments. Instead of M_0, we use the equivalent ratio ${Q_0}^2/d$. In Landel *et al.* (2012), we found $M_0 \approx \langle\overline{M}\rangle = 0.55\left({Q_0}^2/d\right)$, where $\langle\overline{M}\rangle$ is the space- and time-averaged momentum flux in quasi-two-dimensional jets. In particular, the non-dimensional similarity variable $\eta = z/\left(t^{2/3}{M_0}^{1/3}\right)$, defined in the model (see § 3.1), is replaced by $\eta_{exp} = z/\left(t^{2/3}\left({Q_0}^2/d\right)^{1/3}\right)$, so that

$$\frac{\eta_{exp}}{\eta} = \left(\frac{M_0 d}{{Q_0}^2}\right)^{1/3} \approx 0.82. \tag{5.2}$$

This non-dimensionalization also affects the advection and dispersion parameters K_a and K_d, defined in the model (see § 2). As a consequence, the advection and dispersion parameters $K_{a,exp}$ and $K_{d,exp}$, that we use in this section, are related to K_a and K_d as follows:

$$\frac{K_{a,exp}}{K_a} = \frac{K_{d,exp}}{K_d} = \left(\frac{M_0 d}{{Q_0}^2}\right)^{1/2} \approx 0.74. \tag{5.3}$$

We omit the subscript exp in η_{exp}, $K_{a,exp}$ and $K_{d,exp}$ hereafter in this section.

To test our turbulent model hypothesis developed in § 2 and which led to the general effective advection–diffusion (2.5), we choose to compare the theoretical predictions, developed in § 3, first with experiments realized in the constant-flux case. The initial boundary and integral conditions (3.8*a–c*) imposed in the constant-flux case are simpler to satisfy experimentally than the initial boundary and integral conditions imposed in the finite-volume case (3.36*a–c*), which require an instantaneous release of finite volumes of tracers. Instantaneous finite-volume releases of virtual particles are then tested against the theoretical prediction, before studying the more challenging case of a non-instantaneous finite-volume release of dye. In each case, we are particularly interested in whether the natural scaling of the model $z \propto t^{2/3}$ agrees with the experimental results and, if so, we then estimate from the experimental data the two key parameters: the advection parameter K_a and the dispersion parameter K_d. Since the experiments in the constant-flux case are simpler to realize, we believe that the estimates of K_a and K_d measured in this case are more accurate than in the other two cases. Therefore, we consider the values of K_a and K_d measured in the constant-flux case as reference values, while the values measured in the other two cases are used to determine the confidence interval of K_a and K_d. Before presenting the quantitative experimental results, we give below a qualitative assessment of our turbulent model hypothesis and motivate the utility of the new, yet complementary, virtual particle tracking technique (described in § 4.2) in understanding the transport, dispersion and mixing properties of quasi-two-dimensional jets.

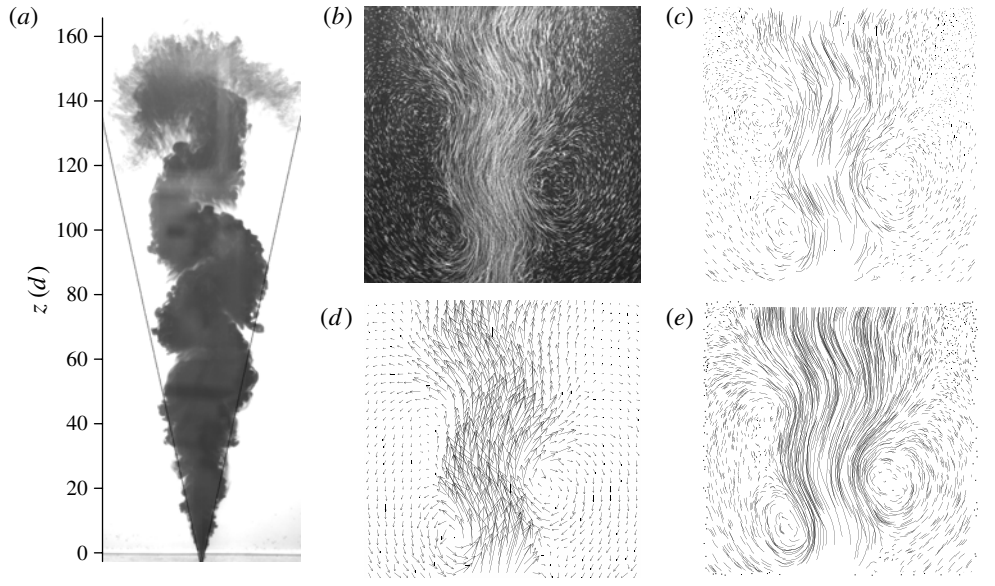

FIGURE 9. (*a*) Grey-scale picture of a dyed jet ($Re_j = 3850$) rising in the tank. The average dye edges are plotted with black lines (half-spreading angle, $\langle\theta_{dye}\rangle = 12.4°$, Landel *et al.* 2012). (*b*) Passive tracers (Pliolite particles) shown as streaks in a typical jet ($Re_j = 4080$). (*c*) Trajectories of the passive tracers shown in (*b*) and identified by imaging analysis (for a duration of 0.2 s). (*d*) Instantaneous velocity field (arrows) of the jet shown in (*b*). (*e*) Trajectories of virtual particles (for approximately 0.3 s) seeded at the same initial locations as the particles identified in (*c*) and evolving as passive tracers in the time-dependent velocity field shown in (*d*).

5.1. *Qualitative assessment*

The purpose of this qualitative assessment is twofold. Firstly, we want to study how the dynamical structure of steady turbulent quasi-two-dimensional jets affects their transport and dispersion properties. We have developed our turbulent model hypothesis, stated in § 2, from the qualitative understanding of these properties. Secondly, we use in this study a new complementary technique to analyse the transport and dispersion properties of the jets, which we introduced in the previous section as virtual particle tracking. We give a qualitative overview of this technique, as well as some justifications and motivations for its use in a more systematic and rigorous approach to obtain quantitative results (which will be presented in § 5.3).

In the far field of quasi-two-dimensional jets, i.e. $z \geqslant 20\,d$ for $W = 2\,d$ (Dracos *et al.* 1992), the core forms a high-speed undulating region, which grows on average in an expanding straight-sided triangular section. Outside the core we observe large counter-rotating eddies, which develop on alternate sides of the core and grow linearly with distance. Moreover, we showed in Landel *et al.* (2012) that the core–eddy structure is self-similar with distance z. The characteristic sinuous core and the large growing eddies can be observed in figure 9(*a*), which is an instantaneous grey-scale picture of a constant-flux release of dye in a steady-state quasi-two-dimensional jet with $Re_j = 3850$ (shown five seconds after injection; the average dye edges are plotted with black lines, half-spreading angle $\langle\theta_{dye}\rangle = 12.4°$, Landel *et al.* 2012). The instantaneous core–eddy structure can also be seen in figure 9(*b*). In figure 9(*b*), a superposition of 50 images (i.e. for a duration of 0.2 s) of the filming of an experiment (obtained

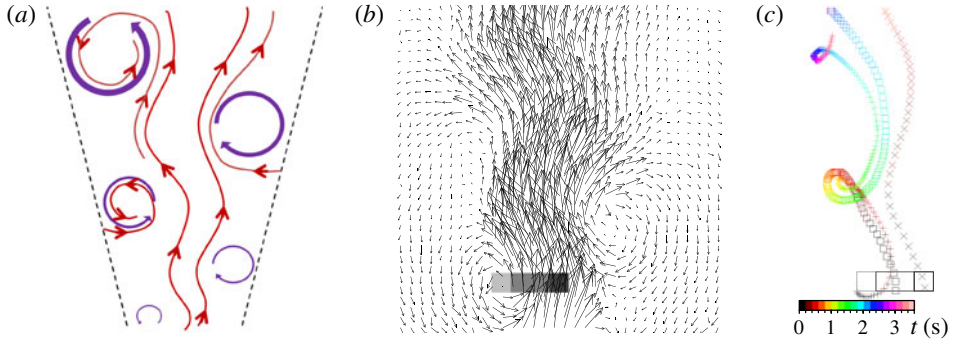

FIGURE 10. (*a*) Schematic diagram describing the structure of quasi-two-dimensional jets. (*b*) Instantaneous velocity field displayed in figure 9(*d*) with three rectangular clusters of virtual particles initially seeded: at the centre of an eddy (plotted in light grey); between the eddy and the core (plotted in grey); and in the core of the jet (plotted in dark grey). (*c*) Typical trajectories of three virtual particles evolving in the time-dependent velocity field shown in (*b*) and initially seeded: in an eddy (cluster outlined in light grey) (plotted with pluses); between the eddy and the core (cluster outlined in grey) (plotted with squares); and in the core (cluster outlined in dark grey) (plotted with crosses). The particle locations are plotted every 0.02 s and each colour corresponds to a time period of 0.2 s (see colour scale).

in our previous study, Landel *et al.* 2012), where passive tracers (0.23 mm Pliolite VTAC particles) were mixed with a quasi-two-dimensional jet ($Re_j = 4080$), depicts the tracers as streaks, thus revealing the Eulerian structures in the flow (see Landel *et al.* 2012 for more details).

We compute two different types of results from the experiment with passive tracers shown in figure 9(*b*). We can consider the tracers as Lagrangian particles and track their trajectory in time using a particle tracking algorithm implemented in DigiFlow (Dalziel 1992; Sveen & Dalziel 2005). Figure 9(*c*) shows the trajectories identified by the algorithm, at the same time instant as the jet displayed in figure 9(*b*). Particles have been tracked for 50 images (i.e. for a duration of 0.2 s) and reveal very similar flow patterns to the streaks in figure 9(*b*). However, this technique has some limitations, as the number of particles tracked for a certain time period decreases quickly with increasing time period. We also have very little control over the initial distribution of the particles (usually spatially homogeneous), and cannot, for example, reproduce an instantaneous finite-volume release of these particles. To remedy these limitations, we have developed a complementary virtual particle tracking technique, which we presented in § 4.2. We seed in the velocity field (displayed in figure 9*d*) of the experimental jet shown in figure 9(*b*) some virtual particles in order to track their trajectory as they are advected as passive tracers by the flow. As a qualitative validation of this technique, we have seeded the virtual particles so that their initial distribution is identical to the initial distribution of the (real) particles identified in figure 9(*c*). The resulting trajectories of the virtual particles are plotted in figure 9(*e*) for a period of approximately 0.3 s. The trajectories of the virtual particles are very similar to the real trajectories of the particles in figures 9(*b*) and 9(*c*), and thus reveal the same core–eddy structure. We believe that the virtual particle tracking technique can provide meaningful information about the transport and dispersion properties of quasi-two-dimensional jets and complements the dye release experiments.

The schematic diagram displayed in figure 10(*a*) summarizes the structure of quasi-two-dimensional jets. The time-averaged mean picture of quasi-two-dimensional jets

is associated with a triangular shape encapsulating all the flow structures, while the time-dependent picture shows a sinuous core flanked by large growing eddies. We believe that the interaction between the core and the eddies results in large streamwise dispersion as the fluid experiences intense stretching at the interface between the core and the eddies. The eddies also play a crucial role in the entrainment and mixing of ambient fluid. From the observations of dyed jets such as the jet illustrated in figure 9(*a*), we find that fluid can be entrained from the ambient by the eddies and then either drawn within the eddies or incorporated into the core. We also believe that fluid can be exchanged between the eddies and the core. On the other hand, we have not observed any dyed fluid being detrained completely from the jet to the ambient, thus suggesting that there are no dead zones in the flow where jet fluid is completely left behind in the quiescent ambient.

These processes can be revealed by applying the virtual particle tracking technique to the core and the eddies of a quasi-two-dimensional jet. In the velocity field of the jet presented in figure 9(*d*) and reproduced in figure 10(*b*), we seed three clusters of virtual particles. The first cluster, composed of 3721 virtual particles, distributed in a square and initially seeded at the centre of an eddy is shown in light grey in figure 10(*b*). The second cluster, composed of 7381 virtual particles, distributed in a rectangle and initially seeded between the eddy and the core is shown in grey in figure 10(*b*). The last cluster, composed of 3721 virtual particles, distributed in a square and initially seeded in the core of the jet is shown in dark grey in figure 10(*b*). Figure 10(*c*) shows the typical trajectories of one single particle from each cluster. The particle locations are plotted every 0.02 s and each colour corresponds to a time period of 0.2 s (see colour scale). The particle starting in the eddy (plotted with pluses) moves slower than the other two particles and its trajectory forms two loops characteristic of the fact that it is transported within the eddy. The particle starting in the core (plotted with crosses) is transported quickly and has a slightly sinuous trajectory, which is characteristic of the transport within the core. On the other hand, the trajectory of the particle chosen approximately at the interface between the eddy and the core (see Landel *et al.* 2012 for a thorough discussion on the identification of the core and eddy structures) is often more complex (plotted with squares) and can be transported from the core to the eddy, or indeed from the eddy to the core. In the present case the particle starts in the core and is then drawn into the neighbouring eddy as the trajectory forms one loop. This is a simple illustration of the possible exchange of fluid parcels between the different structures.

Figure 11 shows the simultaneous evolution in time of all the particles in the three clusters as they are passively advected by the jet velocity field shown in figure 10(*b*). Each colour corresponds to a particular time instant, starting from black and finishing with white and with a time step of 0.2 s between each colour (we use the same colour scale as in figure 10*c*). Again, we can clearly see that the virtual particles are transported much faster in the core of the jet (see figure 11*c*) than in the eddy (see figure 11*a*). On the other hand, mixing is more intense in the eddy than in the core. The cluster initially seeded in the eddy disintegrates very rapidly compared to the cluster initially seeded in the core. The cluster initially seeded between the eddy and the core (see figure 11*b*) experiences considerable stretching in the streamwise direction (its vertical maximum extent is ten times larger than its horizontal maximum extent after a few time steps), owing to the shear layer at the interface between the core and the eddy. We can notice that some virtual particles are drawn into the eddy while others remain in the core. This emphasizes the time-dependent exchange of fluids between the core and the eddies pointed out above. We can also observe the

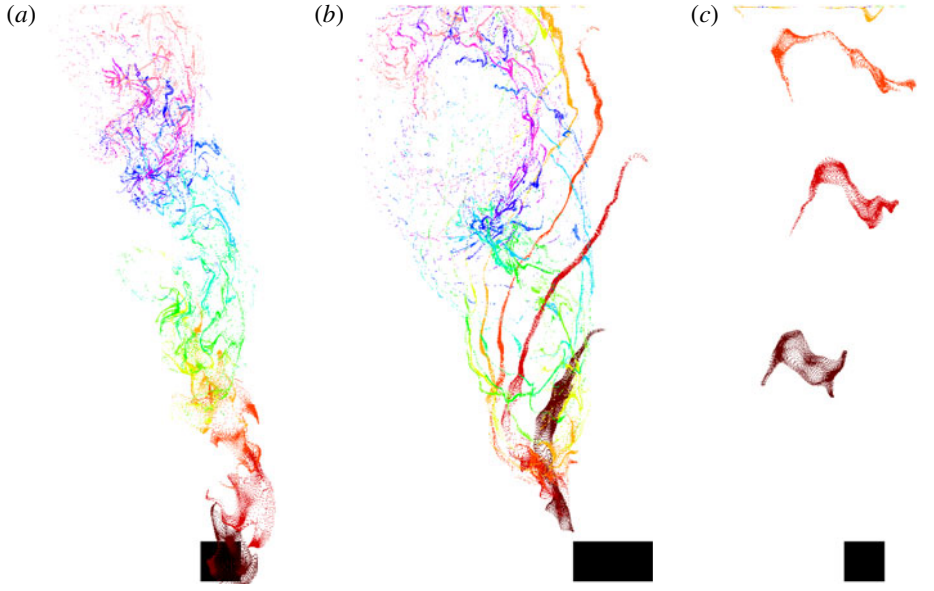

FIGURE 11. Evolution in time of the virtual particles seeded in the velocity field shown in figure 10(*b*) as they are advected by the flow (each colour corresponds to a particular time instant): (*a*) cluster initially distributed at the centre of an eddy and shown in light grey in figure 10(*b*); (*b*) cluster initially distributed between the eddy and the core and shown in grey in figure 10(*b*); (*c*) cluster initially distributed in the core of the jet and shown in dark grey in figure 10(*b*). Each colour corresponds to a time period of 0.2 s, we use the same colour scale as in figure 10(*c*).

delaying effect (with the colour scheme) of the eddies, in which tracers have a longer residency time than in the core.

When ensemble-averaged, we believe that the streamwise dispersive mechanisms revealed by the virtual particles in figure 11 can be modelled as an enhanced dispersion coefficient, as stated in the turbulent hypothesis presented in § 2. The main assumption we make in (2.3), pertaining to the streamwise turbulent eddy diffusion coefficient (i.e. it scales like $b\overline{w}_m$, where b is the jet width, defined in (2.4*a*), and $\overline{w}_m$ is the maximum time-averaged vertical velocity, defined in (2.4*b*)), can be physically justified from the study of both the structures and the velocity profile of quasi-two-dimensional jets (see Landel *et al.* 2012 for velocity measurements in quasi-two-dimensional jets). The core–eddy structure is self-similar with height, thus the local characteristic size of the jet, $b(z)$, appears as a relevant length scale. Moreover, the local maximum time-averaged vertical velocity is the second physically meaningful variable in the problem of dispersion, because all mixing and dispersive mechanisms should scale like $\overline{w}_m(z)$. In the rest of this section, we compare ensemble-averaged experimental results with the theoretical predictions found in § 3 and based on our turbulent model hypothesis.

We believe that the flow in a quasi-two-dimensional jet is appropriate for the application of particle tracking velocimetry because the three-dimensionality of the flow can be considered insignificant in the first order. In § 4.2 we report that the mean divergence of the flow is small compared with the mean vorticity. Moreover, Dracos *et al.* (1992) found that the flow of quasi-two-dimensional jets is primarily

governed by a two-dimensional inverse cascade of turbulence, except at scales of the order of (or less than) the gap width of the tank W. Therefore, we believe that particle tracking velocimetry can give physically meaningful information about the dispersion in quasi-two-dimensional jets. However, we believe that mixing properties cannot be directly examined from the results we present in this study for technical reasons. The measurements of the velocity fields (performed using particle image velocimetry), though well-resolved in time (the time resolution is one order of magnitude smaller than the Kolmogorov time scale, $\tau_{\eta_K} \approx 40$ ms), do not have the spatial accuracy necessary to investigate the finest scales of turbulence in our flow (the Kolmogorov length scale is of the order of $\eta_K \approx 0.2$ mm, as discussed in Landel *et al.* 2012). In fact, we believe that the three-dimensional small-scale turbulence, typically of the order of $W = 1$ cm or less, cannot be adequately resolved in this study, with only a two-dimensional velocity field.

5.2. *Constant-flux releases of dye*

We present in figure 12(*a–c*) experimental results and theoretical predictions of constant-flux releases of dye in quasi-two-dimensional steady turbulent jets. The spatial distribution of the concentration $C(x, z, t)$ is plotted using a colour scale (see colour scale at the top of figure 12*a–c*) at different non-dimensional times, $74 \leqslant \tilde{t} \leqslant 374$, to show the evolution of the dye concentration in the jet. In figure 12(*a*), we plot the ensemble-averaged concentration of the 19 experiments, which were conducted at different jet Reynolds number, $2240 \leqslant Re_j \leqslant 3870$ (see § 4.1). We also plot the average dye edges (half-spreading angle, $\langle\theta_{dye}\rangle = 12.4°$) with thick white lines and the average boundaries of the core (half-spreading angle, 7° starting from $z = 20d$) with thin white lines (Landel *et al.* 2012). We can observe some dispersion of the dye at the leading edge, which indicates the streamwise dispersion discussed above. It is also apparent that the dye is transported first through the core (i.e. within the thin white lines) before mixing across the full width of the jet (i.e. filling the triangle delimited by the average dye edges shown with thick white lines). The characteristic sinuous instability of the core (clearly visible in figure 9*a*) does not appear in figure 12(*a*) because of the averaging process.

Our model is inherently one-dimensional, and so obviously cannot predict the distribution of the concentration across the jet (i.e. in the x-direction). In the partial differential equation (2.3), we consider the concentration integrated along the horizontal axis and study the evolution of $\phi(z, t)$ rather than $C(x, z, t)$. We present the horizontally-integrated experimental concentration $\phi_{F,exp}(z, t)$ in figure 12(*b*) in normalized and redistributed form using

$$C(x, z, t) = \begin{cases} \dfrac{\phi_{F,exp}(z, t)}{2l(z)}, & -l(z) \leqslant x \leqslant l(z), \\ 0, & \text{otherwise}, \end{cases} \tag{5.4}$$

where

$$l(z) = \tan\left(\langle\theta_{dye}\rangle\right)(z - z_0) \quad \text{for } z \geqslant 0 \tag{5.5}$$

is the local horizontal distance between the average dye edges (plotted with thick white lines in figure 12*a*) and z_0 is the space virtual origin defined below in (5.7*a*). Alongside in figure 12(*c*), we show the equivalent theoretical prediction computed from (3.21) for $y_F(\eta)$, based on the assumption of a constant-flux release at the origin of the jet. To compute the theoretical prediction y_F, we use $K_a = 1.65$ and $K_d = 0.09$ for the advection and dispersion parameters, respectively. These parameters

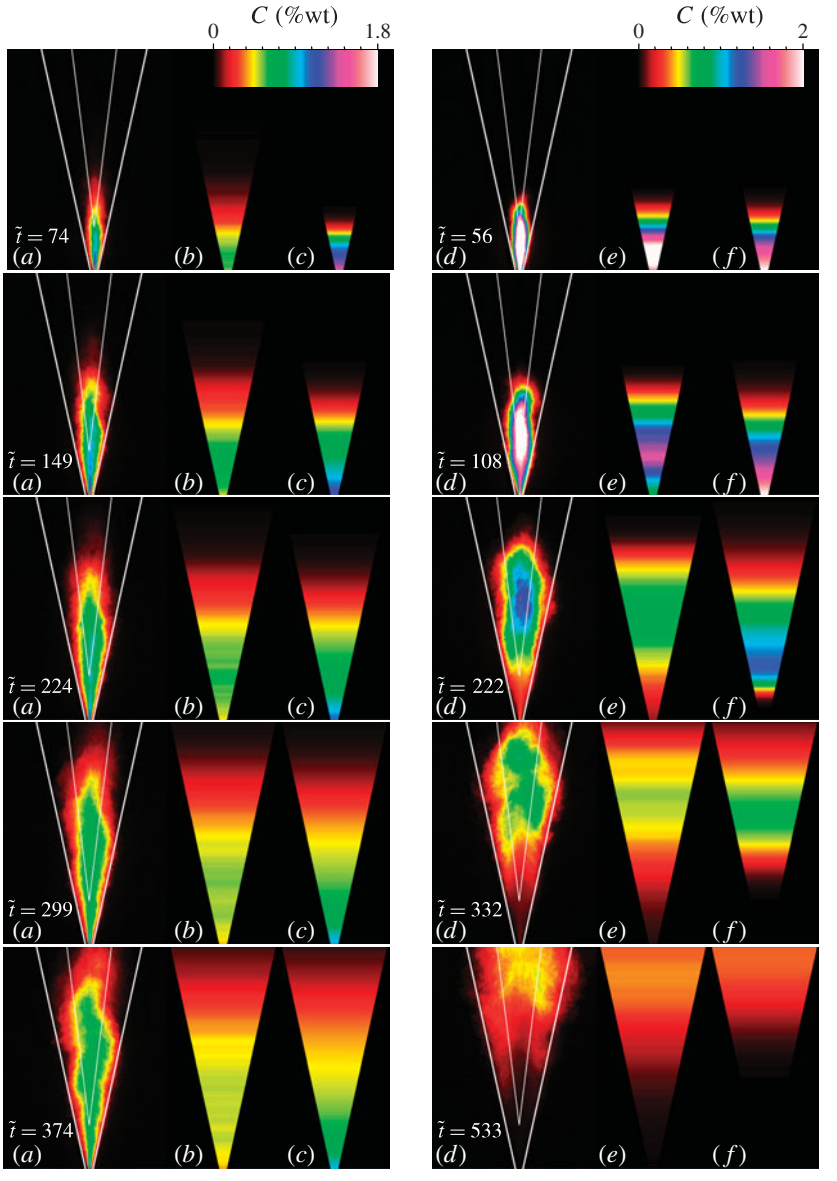

FIGURE 12. Distribution in space and non-dimensional time $\tilde{t} = t/(d^2/Q_0)$ of the concentration of dye (plotted using the two colour scales shown at the top for figures *a–c* and *d–f*, respectively) in the case of constant-flux releases (*a–c*) and finite-volume releases (*d–f*) in turbulent quasi-two-dimensional jets. (*a*) Ensemble average of 19 experiments, the average dye edges plotted with thick white lines (half-spreading angle, $\langle\theta_{dye}\rangle = 12.4°$, Landel *et al.* 2012) and the average boundaries of the core plotted with thin white lines (half-spreading angle, 7° starting from $z = 20d$, Landel *et al.* 2012). (*b*) Spatial horizontal average of the distribution shown in (*a*) (defined in (5.4)). (*c*) Theoretical prediction based on (3.21) and using $K_a = 1.65$ and $K_d = 0.09$. (*d*) Ensemble average of 26 experiments, the average dye edges plotted with thick white lines (half-spreading angle, $\langle\theta_{dye}\rangle = 12.4°$) and the average boundaries of the core plotted with thin white lines (half-spreading angle, 7° starting from $z = 20\,d$). (*e*) Spatial horizontal average of the distribution shown in (*d*) (defined in (5.9)). (*f*) Theoretical prediction based on (3.55) using $K_a = 1.65$, $K_d = 0.09$ and $T_0 = 183(d^2/Q_0)$.

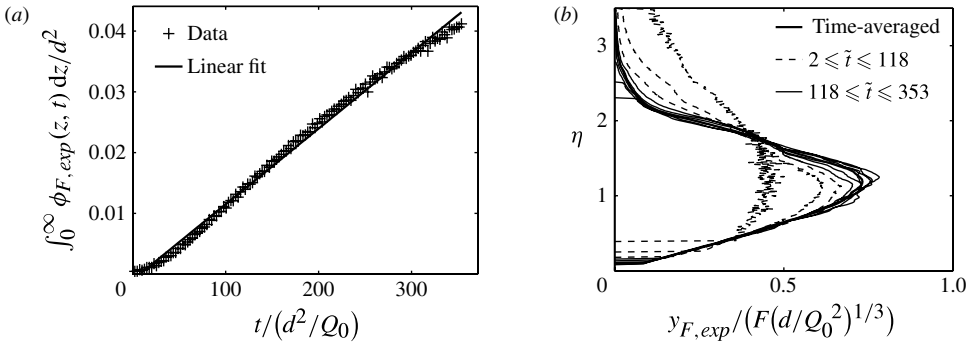

FIGURE 13. (*a*) Evolution in time of the non-dimensional integrated concentration of dye. The experimental data are plotted with pluses, a linear fit is plotted with a black line. (*b*) Evolution in time of the distribution of the normalized ensemble-averaged horizontally-integrated experimental concentration shown in similarity form $y_{F,exp}$ in the case of constant-flux releases (plotted with dashed curves as a function of the similarity variable $\eta = z/\left(t^{2/3}\left(Q_0{}^2/d\right)^{1/3}\right)$ for the time interval $2 \leqslant \tilde{t} \leqslant 118$ and with thin solid curves for the time interval $118 \leqslant \tilde{t} \leqslant 353$). The time-averaged data $\bar{y}_{F,exp}$, for $118 \leqslant \tilde{t} \leqslant 353$, are plotted with a thick solid curve.

are optimized by obtaining the best least-squares fit between the experimental concentration $y_{F,exp}$ (i.e. the similarity form of $\phi_{F,exp}(z,t)$, transformed using (3.9)), and the theoretical prediction y_F. Before plotting the theoretical prediction y_F in figure 12(*c*), we transform y_F into its physical form $\phi_F(z,t)$ using (3.9), then normalize it (similarly to $\phi_{F,exp}(z,t)$) by the local distance $2l(z)$ between the average dye edges, and finally redistribute it uniformly, assuming a top-hat spatially-averaged profile, within these boundaries, i.e.

$$C(x,z,t) = \begin{cases} \dfrac{\phi_F(z,t)}{2l(z)}, & -l(z) \leqslant x \leqslant l(z), \\ 0, & \text{otherwise}, \end{cases} \tag{5.6}$$

where $l(z)$ is defined in (5.5).

Comparing the data (figure 12*b*) with the theoretical prediction (figure 12*c*), we can see that the propagation of the front as well as its dispersion appear to have been correctly modelled (i.e. the scaling is correct), with only a small difference near the source. This mismatch is probably due to the zone of flow establishment of the jet (see e.g. Yannopoulos & Noutsopoulos 1990). There is a necessary time and distance of adjustment before the experimental data can match the theoretical prediction, because the theoretical prediction is based around the assumption that the jet characteristic properties are given by the similarity power laws (2.4*a*,*b*). Giger *et al.* (1991) and Dracos *et al.* (1992) reported that the structure of quasi-two-dimensional jets was different near the source, where three-dimensional effects were important. They found that the self-similar core and eddy structure (which is key in the dispersion mechanisms of the jet) only developed beyond approximately $z \geqslant 20\,d$ (for the aspect ratio $W/d = 2$). Therefore, we might expect our model to be appropriate for $z \geqslant 20d$.

We display in figure 13(*a*) the evolution in time of the non-dimensional integrated concentration of dye released in the experiments shown in figure 12(*a*). We can see that the experimental data (plotted with pluses) increase approximately linearly in time

(a linear fit is plotted with a black line). Therefore, the constant-flux integral condition (3.8*c*) assumed in the model is satisfied experimentally.

We show in figure 13(*b*) the evolution in time of the distribution in similarity space of the normalized experimental data $y_{F,exp}$, plotted for nine successive time periods in the range $2 \leqslant \tilde{t} \leqslant 353$. As we explained earlier, $y_{F,exp}$ is computed from the ensemble-averaged horizontally-integrated experimental concentration for the constant-flux releases $\phi_{F,exp}$ using (3.9) at every instant in time $\tilde{t}$. We also use the following virtual origins in space and time:

$$z_0 = -\frac{{Q_0}^2}{4\sqrt{2}\alpha M_0}, \quad t_0 = \frac{z_0 d}{Q_0}. \tag{5.7a,b}$$

The space virtual origin z_0 is simply the virtual origin of quasi-two-dimensional jets (Landel *et al.* 2012). The time virtual origin t_0 represents the time needed to travel the distance $|z_0|$, from the jet virtual origin to the nozzle, at the average source jet velocity Q_0/d. We shift the origins in space and time from $(z = 0, t = 0)$ (where $z = 0$ corresponds to the height of the nozzle and $t = 0$ corresponds to the time instant when the dye first appears from the nozzle) to (z_0, t_0) by applying the following transformation between the new and old coordinates:

$$z_{new} = z_{old} - z_0, \quad t_{new} = t_{old} - t_0. \tag{5.8a,b}$$

For simplicity, we omit the subscripts 'new' and 'old' hereafter. In Landel *et al.* (2012), we found $\alpha \approx 0.068$ and $M_0 \approx \langle \overline{M} \rangle = 0.55 \left({Q_0}^2/d\right)$. So, the non-dimensional virtual origins in space and time are $\tilde{z}_0 = \tilde{t}_0 \approx -4.7$. Except for the data in the time interval, $2 \leqslant \tilde{t} \leqslant 118$ (plotted with dashed curves), the data corresponding to the time interval, $118 \leqslant \tilde{t} \leqslant 353$ (plotted with thin solid curves), seem to have a similar distribution. The experimental concentration distribution converges rapidly, in time, towards an asymptotic profile in similarity space (y, η). We approximate this asymptotic distribution by the time-averaged distribution $\overline{y}_{F,exp}$ for $118 \leqslant \tilde{t} \leqslant 353$ (plotted with a thick solid curve in figure 13*b*). The rapid convergence of the data in similarity space is very important because it means that the similarity scalings derived from the model, $\phi_F(z, t) = t^{1/3} y_F(\eta)$ (with $\eta \propto z/t^{2/3}$), are the appropriate scalings for this phenomenon. We can notice in figure 13(*b*) that near $\eta = 0$ the data are incomplete. Small values of $\eta \propto z/t^{2/3}$ are equivalent to small values of z compared with $t^{2/3}$, or large values of $t^{2/3}$ compared with z. The incomplete data near $\eta = 0$ are simply due to a lack of spatial resolution near the source and a finite time of observation in the experiments.

We present the experimental data $\overline{y}_{F,exp}$ in figure 14 (the ensemble average is plotted with pluses and the standard deviation, STD, with dotted curves). We compute the best least-squares fit using the theoretical formula (3.21), where K_a and K_d are optimized under the constant-flux constraint (3.11*b*). The best fit (plotted with a solid curve) is found for $K_a = 1.65$ and $K_d = 0.09$. We can see that the model captures the main characteristics of the data. The concentration increases from zero at the origin (where the first derivative is infinite) to a peak value and then decreases smoothly at the front. The front of the curve agrees with the theoretical fit, and so the dispersion processes appears to have been correctly modelled. The rear of the experimental data appears slightly more linear than the theoretical prediction. This mismatch is probably due to the zone of flow establishment discussed above.

The ratio between the advection parameter and the dispersion parameter is approximately $K_d/K_a = 0.055$. Using the advection parameter, we can compute

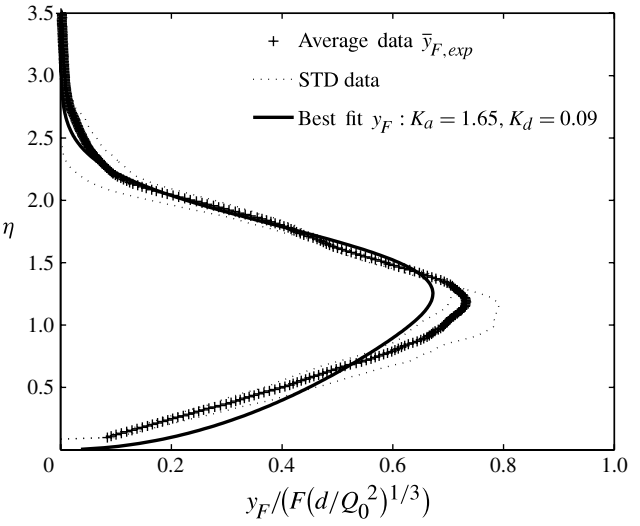

FIGURE 14. Constant-flux case, in similarity form. Plots of the ensemble average (pluses) and standard deviation (STD) (thin dotted curves) of the normalized experimental dye concentration $\bar{y}_{F,exp}$ (pluses) and best least-squares fit using y_F from (3.21) and with $K_a = 1.65$ and $K_d = 0.09$ (solid curve) as a function of the similarity variable $\eta = z/\left(t^{2/3}\left(Q_0{}^2/d\right)^{1/3}\right)$.

theoretically the location of the advective front (considering 'top-hat' mean velocity profiles in the jet with no turbulent dispersion), $\eta_a = 1.83$, based on (3.24). We can also measure from the experimental data the portion of the dye which travels ahead of the advective front $\beta_{F,exp} = 0.12$ (computed using (3.26)), which is close to the theoretical prediction $\beta_F = 0.10$ (shown with a cross in figure 2*a*) based on the ratio $K_d/K_a = 0.055$ and using (3.27). Thus, at each instant in time a non-negligible proportion of the total volume of tracers having been released travels ahead of the advective front η_a. Finally, we can also determine from the experimental data the normalized distance between the average location of the volume of tracers travelling ahead of the advective front and the location of the advective front η_a, $\xi_{F,exp} = 0.16$ (computed using (3.28)). This value is larger than the theoretical prediction based on the ratio $K_d/K_a = 0.055$ and using (3.29), $\xi_F = 0.13$ (shown with a cross in figure 2*b*). Here ξ_F is a measure of the spread of the front of the distribution compared with the distance of the peak from the origin.

All these agreements between the data $\bar{y}_{F,exp}$ and the best least-squares fit y_F suggest that our model can predict the shape of the concentration distribution of a finite-volume release of tracers in quasi-two-dimensional jets. We believe that the constant-flux experiments are the most straightforward experiments performed in this study. Therefore, the values of the advection and the dispersion parameters $K_a = 1.65$ and $K_d = 0.09$, respectively, found in this case will be used in the next cases as reference values. Furthermore, these results clearly reveal the importance of dispersion processes in the transport of passive tracers by quasi-two-dimensional jets. As is clear in figure 14, the front of the distribution of the concentration in the similarity space (y, η) is not sharp but smooth due to dispersion. Were the transport of passive tracers by quasi-two-dimensional jets purely governed by advective processes alone, in the sense of a 'top-hat' mean velocity profile in the jet with $K_d \to 0$ and with no parametrized streamwise turbulent dispersion, the distribution of the concentration

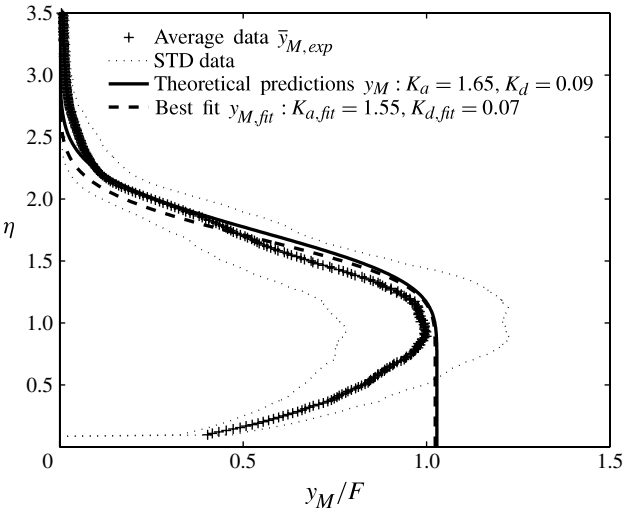

FIGURE 15. Constant-flux case, in similarity form. Plots of the ensemble average (pluses) and standard deviation (STD) (thin dotted curves) of normalized experimental dye flux $\overline{y}_{M,exp}$, theoretical prediction y_M using (3.30) and with $K_a = 1.65$ and $K_d = 0.09$ (solid curve), and best least-squares fit $y_{M,fit}$ using (3.30) and with $K_{a,fit} = 1.55$ and $K_{d,fit} = 0.07$ (dashed curve) as a function of the similarity variable $\eta = z/\left(t^{2/3}\left({Q_0}^2/d\right)^{1/3}\right)$.

in similarity space would drop much more rapidly at the front, as shown by the distributions of $y_{F,a}$ in figure 1 (plotted with a thin solid curve and a thin dashed curve). It is also important to note that more than 10 % of the total volume of tracers released, at any time, propagates ahead of the advective front.

We plot the normalized ensemble-averaged experimental results for the concentration flux of dye $\overline{y}_{M,exp}/F$ in figure 15 with pluses, while the standard deviation of the data (STD) is plotted with thin dotted curves. The experimental concentration flux of dye $M_{\phi,exp}$ is computed using the expression (2.5*b*) with $K_a = 1.65$, as found above for the best fit of $\overline{y}_{F,exp}$ in the constant-flux case (see figure 14), and the virtual origins described in (5.7*a*,*b*). Then, according to (3.30), the similarity form is $\overline{y}_{M,exp} = M_{\phi,exp}$. We compute the theoretical prediction y_M (plotted with a solid curve) using the theoretical formula (3.30) with $K_a = 1.65$ and $K_d = 0.09$, the reference values obtained in the constant-flux case for y_F (see figure 14). We also compute the best least-squares fit $y_{M,fit}$ using the theoretical formula (3.30), where $K_{a,fit}$ and $K_{d,fit}$ are optimized. The best fit (plotted with a dashed curve) is found for $K_{a,fit} = 1.55$ and $K_{d,fit} = 0.07$. Indeed, the values of the advection and dispersion parameters for the best fit and the theoretical prediction are actually very similar. The theoretical prediction matches with the data at the front, with the dispersion processes appearing to have been correctly modelled, but near the origin the data drop towards zero instead of remaining constant. The absence of a plateau near the origin in the experimental results is presumably due to the time and distance of adjustment before the experimental data can match the theoretical prediction, which we mentioned previously as being associated with the zone of flow establishment.

We can measure from the experimental data the proportion of the dye flux being ahead of the advective front $\beta_{M,exp} = 0.09$ (computed using (3.32)), which is close to the theoretical prediction $\beta_M = 0.06$ (shown with a cross in figure 4*a*) based

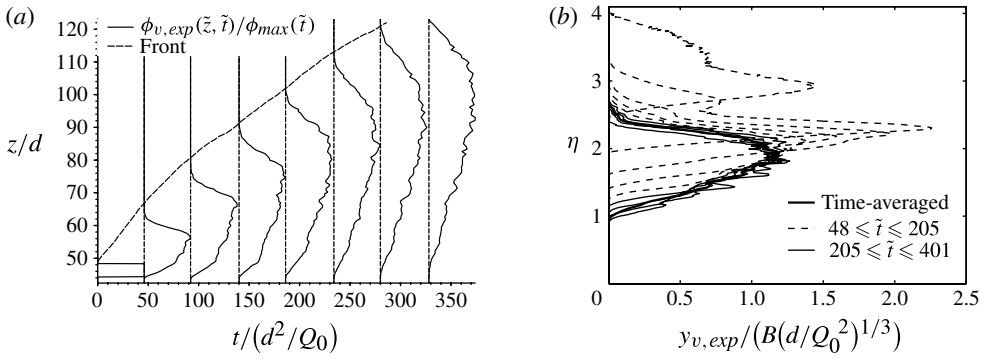

FIGURE 16. (*a*) Vertical distribution of the normalized horizontally-integrated concentration of virtual particles $\phi_{v,exp}(z,t)/\phi_{max}(t)$ (plotted with solid curves) at different non-dimensional times. The results have been averaged for 256 releases of identical clusters in the velocity fields of quasi-two-dimensional turbulent jets of source volume flow rates 33.2, 37.0 and 40.3 cm^3 s^{-1}. The location of the front of the ensemble-averaged cluster is plotted as a function of time with a thick dashed curve. (*b*) Evolution in time of the distribution in similarity form of the normalized ensemble-averaged horizontally-integrated experimental concentration of virtual particles $y_{v,exp}$ (plotted with dashed curves for the time interval $48 \leqslant \tilde{t} \leqslant 205$ and with thin solid curves for the time intervals $205 \leqslant \tilde{t} \leqslant 401$) as a function of the similarity variable $\eta = z/\left(t^{2/3}(Q_0{}^2/d)^{1/3}\right)$. The time-averaged data $\bar{y}_{v,exp}$, for $205 \leqslant \tilde{t} \leqslant 401$, are plotted with a thick solid curve.

on the ratio $K_d/K_a = 0.055$ and using (3.33). We can also determine from the experimental data the normalized distance between the average location of the volume of tracers travelling ahead of the advective front and the location of the advective front (considering 'top-hat' mean velocity profiles in the jet with no turbulent dispersion) η_a, $\xi_{M,exp} = 0.19$ (computed using (3.34)). This value is somewhat larger than the theoretical prediction based on the ratio $K_d/K_a = 0.055$ and using (3.35), $\xi_M = 0.12$ (shown with a cross in figure 4*b*).

The study of the flux of dye in the constant-flux case also demonstrates the ability of the model to predict both advective and diffusive processes. It is clear from the observation of the front of the profile in figure 15 that quasi-two-dimensional jets diffuse tracers in a qualitatively different manner from the 'top-hat' purely advective case $y_{M,a}$ presented in figure 3 (plotted with a thin solid curve and a thin dashed curve). Moreover, we measure that approximately 10 % of the total concentration flux of tracers is located ahead of the advective front.

5.3. *Instantaneous finite-volume releases of virtual particles*

We now compare our effective advection–diffusion model with experiments conducted using finite-volume releases of tracers in quasi-two-dimensional jets. The initial boundary and integral conditions imposed in the finite-volume case (3.36*a–c*) are more difficult to reproduce experimentally because they require an instantaneous release. As we discussed in § 4.3, an instantaneous release is not physically possible in laboratory experiments, but it can be achieved using virtual particles. So, we first investigate the case of finite volumes of virtual particles released in the velocity field of quasi-two-dimensional jets, before analysing the more difficult problem of finite-volume releases of dye, presented in § 5.4.

We show in figure 16(*a*) the non-dimensionalized vertical distribution, at eight different times, of the horizontally-integrated normalized concentration $\phi_{v,exp}(\tilde{z},\tilde{t})/\phi_{max}(\tilde{t})$ (where $\phi_{max}(\tilde{t})$ is the maximum value of $\phi_{v,exp}(\tilde{z},\tilde{t})$ in time, and $\tilde{z}=z/d$ and $\tilde{t}=t/(d^2/Q_0)$ as defined in (5.1*a*,*b*), respectively) of the ensemble average of 256 virtual particle clusters released instantaneously, as finite volumes, in the experimental velocity field of quasi-two-dimensional jets with source volume flow rates 33.2, 37.0 and 40.3 cm^3 s^{-1} (see § 4.2). At each time, we bin the data into one hundred evenly-spaced intervals extending from the origin to the maximum vertical extent of the ensemble-averaged cluster. The thick dashed curve shows the location of the front z_f of the ensemble-averaged cluster in time, which reaches the top boundary of the velocity field at approximately $\tilde{t}=290$, after the release time. The location of the front follows the expected power law $z_f \propto t^{2/3}$ (Landel *et al.* 2012). As we can see, the ensemble-averaged cluster rapidly changes from an initial rectangular shape to a smoother rounded profile as it is advected by the jet. At early times $\tilde{t}\leqslant 150$, the dispersion of the particles appears to differ slightly between the front and the rear of the ensemble-averaged cluster. The front is sharper and drops more rapidly, while the rear has a longer tail. This is probably due to the fact that at the beginning most particles are advected quickly by the core of the jet, while the rest are trapped in the lateral eddies where they move more slowly. As reported in Landel *et al.* (2012), the time-averaged vertical speed of an eddy is approximately 25 % of the maximum speed of the core. However, at later times the cluster seems to spread more symmetrically between the front and the rear. We believe this is due to the continuous exchange of material between the core and the eddies.

We apply the similarity transformation (3.37) to the ensemble-averaged experimental concentration $\phi_{v,exp}$ to obtain the similarity form $y_{v,exp}$, normalized by the total volume of virtual particles $B_{v,exp}=2\,624\,256$. We use the space virtual origin z_0 defined in (5.7*a*). The time virtual origin cannot be the same as defined in the simple (5.7*b*) because the jet velocity is not constant between the jet virtual origin z_0 and the location of release of the virtual particles (i.e. $44.4\leqslant z/d\leqslant 48.3$). We determine the time virtual origin so that the location of the front in time $\tilde{z}_f(\tilde{t})$ (plotted with a thick dashed curve in figure 16*a*) best fits (using a least-squares fit) a straight line in a log–log plot. We show in figure 16(*b*) the evolution in time of the distribution in similarity space of the normalized experimental data $y_{v,exp}$, plotted for nine successive time periods in the range $48\leqslant\tilde{t}\leqslant 401$. We can see that $y_{v,exp}$ seems to converge towards an asymptotic distribution after $205\leqslant\tilde{t}$. To illustrate this, the data for $48\leqslant\tilde{t}\leqslant 205$ are plotted with dashed curves, while the data for $205\leqslant\tilde{t}\leqslant 401$ are plotted with thin solid curves. We approximate the asymptotic distribution by the time-averaged distribution $\overline{y}_{v,exp}$ for $205\leqslant\tilde{t}\leqslant 401$ (plotted with a thick solid curve in figure 16*b*). Similarly to the constant-flux case, the convergence of these finite-volume data in similarity space implies that the similarity scalings derived from the model, $\phi_\delta(z,t)=t^{-2/3}y_\delta(\eta)$ (with $\eta\propto z/t^{2/3}$), are the appropriate scalings for this phenomenon.

In figure 17, we compare the time-averaged ensemble-averaged virtual particle data $\overline{y}_{v,exp}$ with the theoretical prediction of the fundamental solution y_δ (plotted with a solid curve), which assumes an instantaneous release. The ensemble average is plotted with crosses and the standard deviation, STD, is plotted with dotted curves. We compute the theoretical prediction y_δ using (3.44) with $K_a=1.65$ and $K_d=0.09$, the reference values obtained in the constant-flux case for y_F (see figure 14). We also compute the best least-squares fit $y_{\delta,fit}$ (plotted with a dashed curve in figure 17) using (3.44), where $K_{a,fit}$ and $K_{d,fit}$ are optimized under the finite-volume constraint (3.39*b*).

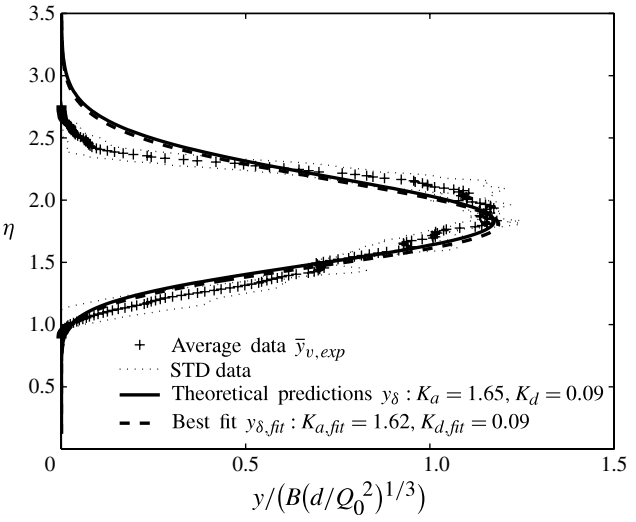

FIGURE 17. Finite-volume case, instantaneous release, in similarity form. Plots of the variation with similarity variable $\eta = z/\left(t^{2/3}\left(Q_0{}^2/d\right)^{1/3}\right)$ of the ensemble average (plotted with pluses) and standard deviation (STD) (plotted with thin dotted curves) of the normalized time-averaged experimental concentration of virtual particles $\bar{y}_{v,exp}$ (plotted with pluses), theoretical prediction y_δ defined by (3.44) with $K_a = 1.65$ and $K_d = 0.09$ (plotted with a solid curve), and best least-squares fit using $y_{\delta,fit}$ defined by (3.44) with $K_{a,fit} = 1.62$ and $K_{d,fit} = 0.09$ (plotted with a dashed curve).

The best least-squares fit between $\bar{y}_{v,exp}$ and $y_{\delta,fit}$ is obtained for $K_{a,fit} = 1.62$ and $K_{d,fit} = 0.09$. Once again, these best-fit values are quite similar to the reference values.

We can see that the model captures the main characteristics of the data. The concentration increases from zero at the origin (where the first and second derivatives also vanish) to a peak value and then decreases at the front, following the theoretical prediction y_δ. The location of the peak of $\bar{y}_{v,exp}$, which is also the location of the advective front, is at $\eta_{a,exp} = 1.83$. Using the advection parameter $K_a = 1.65$, we can compute theoretically a very similar value $\eta_a = 1.83$, based on (3.24). We can also measure from the experimental data the portion of the virtual particles which travels ahead of the advective front $\beta_{B,exp} = 0.49$ (computed using (3.47)), which is very close to the theoretical prediction $\beta_B = 0.54$ (shown with a cross in figure 6*a*) based on the ratio $K_d/K_a = 0.055$ and using (3.48). (A value β_B of 0.5 means that the virtual particles are symmetrically distributed with respect to the concentration peak.) Finally, we can also determine from the experimental data the normalized distance between the average location of the volume of tracers travelling ahead of the advective front and the location of the advective front (considering 'top-hat' mean velocity profiles in the jet with no parametrized streamwise turbulent dispersion) η_a, $\xi_{B,exp} = 0.13$ (computed using (3.49)). This value is somewhat smaller than the theoretical prediction based on the ratio $K_d/K_a = 0.055$ and using (3.50), $\xi_B = 0.17$ (shown with a cross in figure 6*b*). Here ξ_B is a measure of the spread of the distribution compared with the distance of the peak from the origin.

All these agreements between the data $\bar{y}_{v,exp}$ and the theoretical prediction y_δ, and between the advection and dispersion parameters of the constant-flux case and the finite-volume case, suggest that our model can predict the shape of the

concentration distribution of an instantaneous finite-volume release of tracers in quasi-two-dimensional jets. Furthermore, it clearly reveals the importance of dispersion processes in the transport of passive tracers by quasi-two-dimensional jets. As is clear in figure 16(*b*), the distribution of the concentration in the similarity space (y, η) converges in time towards a distribution with a finite width. Were the transport of passive tracers by quasi-two-dimensional jets purely governed by advective processes alone (i.e. in the sense of a 'top-hat' mean velocity profile in the jet with no turbulent dispersion), the distribution of the concentration in similarity space would rather shrink towards a distribution of negligible width (similar to a Dirac delta function), even with a non-instantaneous release of tracers. It is also important to note that approximately half of the total volume of tracers in figure 17 travels ahead of the advective front, at a normalized averaged distance $\xi_B \approx 0.17$ (defined in (3.50) with $K_d/K_a = 0.055$).

5.4. *Finite-volume releases of dye*

We also present in figure 12(*d–f*) experimental results and theoretical predictions of finite-volume releases of dye in quasi-two-dimensional steady turbulent jets. The spatial distribution of the concentration $C(x, z, t)$ is plotted using a colour scale (see colour scale at the top of figure 12*d–f*) at different non-dimensional times, $56 \leqslant \tilde{t} \leqslant 533$, to show the evolution of the patch of dye as it is advected, mixed and dispersed by the jet. In figure 12(*d*) we plot the ensemble average of the 26 experiments, which were conducted at different jet Reynolds numbers, $2170 \leqslant Re_j \leqslant 4870$ (see § 4.3). We also plot the average dye edges (half-spreading angle, $\langle\theta_{dye}\rangle = 12.4°$) with thick white lines and the average boundaries of the 'core' (half-spreading angle, 7° starting from $z = 20d$) with thin white lines (Landel *et al.* 2012). Similarly to the constant-flux results presented in figure 12(*a–c*), we can observe that the interaction between the core and the eddies, as described in Landel *et al.* (2012), results in large streamwise dispersion. As we explained earlier, we model this streamwise dispersion using an enhanced turbulent eddy diffusion coefficient which scales like $b\overline{w}_m$.

We present the horizontally-integrated experimental concentration $\phi_{B,exp}(z, t)$ in figure 12(*e*) in normalized and redistributed form using

$$C(x, z, t) = \begin{cases} \dfrac{\phi_{B,exp}(z, t)}{2l(z)}, & -l(z) \leqslant x \leqslant l(z), \\ 0, & \text{otherwise}, \end{cases} \tag{5.9}$$

where $l(z) = \tan(\langle\theta_{dye}\rangle)(z - z_0)$, as defined in (5.5), is the local horizontal distance between the average dye edges (plotted with thick white lines in figure 12*d*), and z_0 is the space virtual origin defined in (5.7*a*). Alongside in figure 12(*f*), we show the equivalent theoretical prediction $\phi_{T_0}(z, t)$ computed from (3.55) and based on the assumption of a finite volume being released at a constant-flux during a finite period of time $T_0 = 183\ \left(d^2/Q_0\right)$. We discuss this particular value in more detail below. To compute ϕ_{T_0}, we use $K_a = 1.65$ and $K_d = 0.09$ for the advection and dispersion parameters, respectively, the reference values obtained in the constant-flux case for y_F (see figure 14). Before plotting the theoretical prediction ϕ_{T_0} in figure 12(*f*), we normalize it (similarly to $\phi_{B,exp}(z, t)$) by the local distance $2l(z)$ between the average dye edges, and finally redistribute it uniformly, assuming a top-hat spatially-averaged profile, within these boundaries, i.e.

$$C(x, z, t) = \begin{cases} \dfrac{\phi_{T_0}(z, t)}{2l(z)}, & -l(z) \leqslant x \leqslant l(z), \\ 0, & \text{otherwise}, \end{cases} \tag{5.10}$$

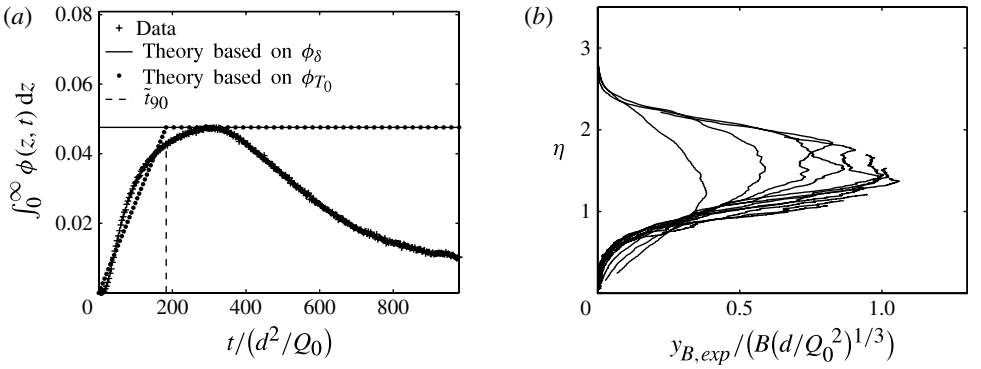

FIGURE 18. (*a*) Evolution in time of the integral of the dye concentration over the whole domain for: the experimental data $\phi_{B,exp}$ (plotted with pluses); the theoretical prediction ϕ_δ (plotted with a solid line), defined by (3.44); and the theoretical prediction ϕ_{T_0} (plotted with a dotted line), defined by (3.55). The dashed line indicates the time instant $\tilde{t}_{90} = 183$ when approximately 90 % of the total integrated concentration of dye ('seen' by the imaging analysis) has entered the tank. (*b*) Plots of the variation with similarity variable $\eta = z/\left(t^{2/3}\left(Q_0{}^2/d\right)\right)$ of the evolution in time of the normalized ensemble-averaged horizontally-integrated experimental concentration plotted in similarity form, $y_{B,exp}$ (computed from $\phi_{B,exp}$ using (3.37)), in the case of finite-volume releases of dye. The data are plotted at 12 different time instants for $0 \leqslant \tilde{t} \leqslant 979$, with time increasing as the amplitude of the data increases.

where $l(z)$ is defined in (5.5).

Although the comparison between the experimental data in figure 12(*e*) and the theoretical prediction in figure 12(*f*) is not perfect at early times and near the origin, as the theoretical concentration seems to travel slightly slower than the experimental concentration for $\tilde{t} \leqslant 222$, it improves at later times as the jet advects and diffuses the dye. As we mentioned above, this mismatch is probably due to the zone of flow establishment of the jet. There is a necessary time and distance of adjustment before the experimental data can match the theoretical prediction, because the theoretical prediction is based around the assumption that the jet characteristic properties are given by the similarity power laws (2.4*a*,*b*).

In these experiments, we naturally are not able to release finite volumes of dye instantaneously. Aspects of the experimental dye release are revealed in figure 18(*a*), where we show the evolution in time of the integral of the dye concentration over the whole domain $\int_0^\infty \phi_{B,exp}(z,t)\,\mathrm{d}z$ (plotted with pluses). These data represent the total volume of dye 'seen' by the imaging analysis in the window frame $-40 \leqslant x/d \leqslant 40$ and $0 \leqslant z/d \leqslant 100$. The dashed line indicates the time instant $\tilde{t}_{90} = 183$, when approximately 90 % of the total volume of dye 'seen' by the imaging analysis has entered the tank. We can see that the total volume of dye increases almost steadily for $\tilde{t} \leqslant \tilde{t}_{90}$. Then, the total volume of dye reaches a maximum at $\tilde{t} \approx 290$ before decreasing smoothly as the dye is transported outside the window frame. These data clearly show that the release of dye occurs over a finite period of time and is not instantaneous.

The effect of the spreading in time of the release of dye can also be seen in the evolution in time of the concentration distribution in the jets. In figure 18(*b*), we show the non-dimensional experimental concentration in similarity form $y_{B,exp}$ (computed from $\phi_{B,exp}$ using (3.37) at each instant in time). We normalize $y_{B,exp}$ by the total

injected volume B and plot it at 12 different instants in time for $0 \leqslant \tilde{t} \leqslant 979$, with time increasing as the amplitude of the data increases. The space and time virtual origins described in (5.7*a*,*b*) are used to compute $y_{B,exp}$. Ideally, if the dye were released instantaneously at the origin, as described in the integral and initial boundary conditions (3.36*a*–*c*), all the curves should be identical and collapse on a single profile. Instead, we observe a gradual increase of the area under the curves. The data do not appear to have yet reached an asymptotic distribution. It can also be noticed that the curves at late times (for $290 \leqslant \tilde{t}$) are not plotted over the whole range $0 \leqslant \eta \leqslant 3.5$, but stop at some values $\eta < 3.5$. These curves are incomplete because for $290 \leqslant \tilde{t}$, the front of the dye located at the height z_f has already moved outside the image frame, i.e. $z_f/d > 100$, and thus we cannot visualize the full distribution of the dye in space.

It is clear from both figures 18(*a*,*b*) that the release of the dye is not instantaneous and that the data have not yet reached an asymptotic distribution in similarity space. Thus, we cannot use the theoretical prediction y_δ defined in (3.44) to model these experiments, as we did in the case of finite-volume releases of virtual particles presented above, because the fundamental solution y_δ assumes an instantaneous release of the finite volume of tracers (see the integral and initial boundary conditions (3.36*a*–*c*)). Therefore, we compare the experimental data $\phi_{B,exp}(z,t)$ with the general solution $\phi_g(z,t)$, described in (3.52) and based on the convolution of the fundamental solution ϕ_δ with a source function $f(t) = \phi_g(0,t)$. The source function can model the more general and realistic case of a time-dependent release.

To compute the general solution $\phi_g(z,t)$, we need to define the source function $f(t)$, which represents the rate at which the overall integrated volume of tracers changes with time. In figure 18(*a*), we observe that the total integrated concentration of dye $\int_0^\infty \phi_{B,exp}(z,t)\,\mathrm{d}z$ increases almost linearly with time for $\tilde{t} \leqslant \tilde{t}_{90}$. Hence, we choose to model the source function as simply a non-zero constant for $0 \leqslant \tilde{t} \leqslant \tilde{t}_{90}$ and zero for $\tilde{t}_{90} \leqslant \tilde{t}$:

$$f_{\tilde{t}_{90}}(\tilde{t}) = \frac{H(\tilde{t}) - H(\tilde{t} - \tilde{t}_{90})}{\tilde{t}_{90}}. \tag{5.11}$$

Using such a rectangular source function, the general solution $\phi_g(z,t)$ corresponds to the particular solution ϕ_{T_0} (with $T_0 = t_{90}$), described in (3.55). We plot the resulting theoretical integrated concentration $\int_0^\infty \phi_{T_0}(z,t)\,\mathrm{d}z$ with a dotted curve in figure 18(*a*). We can see that the match with the data (plotted with pluses) is, at least until the dye is advected beyond the spatial range of the camera (for $\tilde{t} \leqslant 290$), better than for the model assuming an instantaneous release ϕ_δ (plotted with a solid line).

We compute the theoretical prediction ϕ_{T_0}, based on the source function $f_{\tilde{t}_{90}}$ with $T_0 = t_{90} = 183(d^2/Q_0)$, using the virtual origins described in (5.7*a*,*b*). We compare the distribution of the experimental data $\phi_{B,exp}$ (plotted with pluses) and the theoretical prediction ϕ_{T_0} (plotted with solid curves) in figure 19 at nine different times for $0 \leqslant \tilde{t} \leqslant 418$. We compute ϕ_{T_0} using the advection and dispersion parameters $K_a = 1.65$ and $K_d = 0.09$, respectively, the reference values obtained in the constant-flux case for y_F (see figure 14). We also show the best least-squares fit $\phi_{T_0,fit}$ (plotted with dashed curves in figure 19), computed using the theoretical formula (3.55) and the source function $f_{\tilde{t}_{90}}$ (see (5.11)) with $T_0 = t_{90} = 183(d^2/Q_0)$. The advection and dispersion parameters $K_{a,fit}$ and $K_{d,fit}$, respectively, are optimized under the finite-volume constraint (3.36*c*). The best least-squares fit between $\phi_{B,exp}$ and $\phi_{T_0,fit}$ is obtained for $K_{a,fit} = 1.75$ and $K_{d,fit} = 0.09$, still quite close to the reference values. Overall, we observe reasonable agreement between ϕ_{T_0} and $\phi_{B,exp}$. At early times,

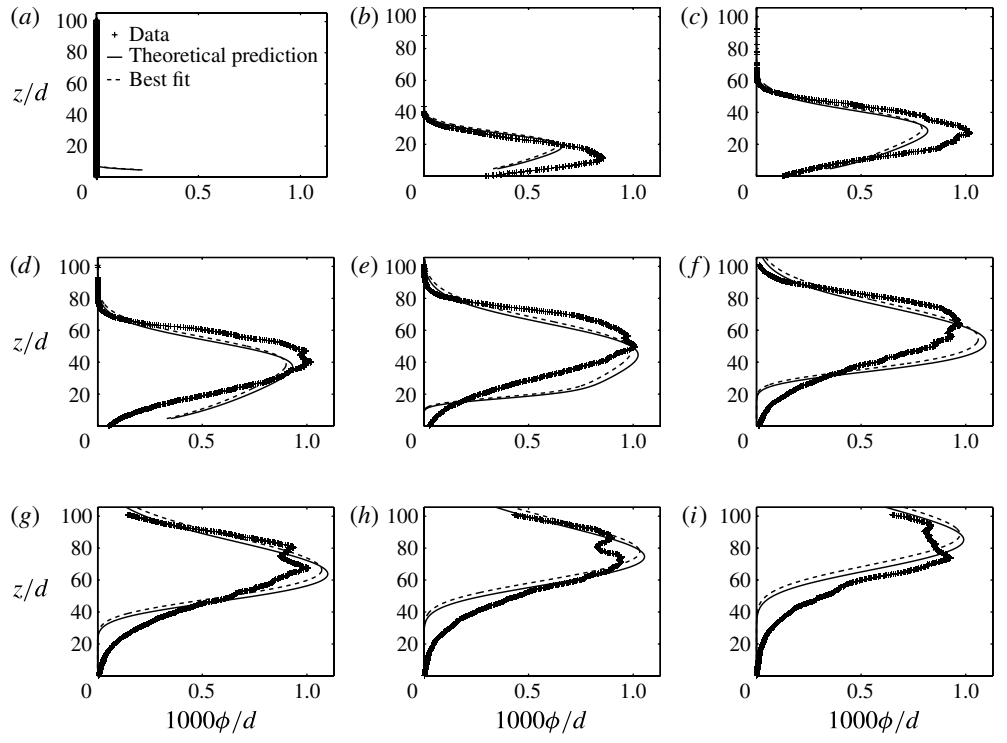

FIGURE 19. Plots at various times of the vertical distribution of the horizontally-integrated concentration of dye as a function of the non-dimensional distance z/d in the case of finite-volume releases for: ensemble-averaged experimental data $\phi_{B,exp}$ (plotted with pluses); theoretical prediction ϕ_{T_0} (plotted with solid curves), based on (3.55) using the reference advection and dispersion parameters $K_a = 1.65$ and $K_d = 0.09$, respectively, and the source function $f_{\tilde{t}_{90}}(t)$ as defined in (5.11); and best least-squares fit $\phi_{T_0,fit}$ (plotted with dashed curves), based on (3.55) using the advection and dispersion parameters $K_{a,fit} = 1.75$ and $K_{d,fit} = 0.09$, respectively, and the source function $f_{\tilde{t}_{90}}(t)$ as defined in (5.11). Times: (*a*) $t/(d^2/Q_0) = 0$, (*b*) $t/(d^2/Q_0) = 51$, (*c*) $t/(d^2/Q_0) = 103$, (*d*) $t/(d^2/Q_0) = 155$, (*e*) $t/(d^2/Q_0) = 207$, (*f*) $t/(d^2/Q_0) = 259$, (*g*) $t/(d^2/Q_0) = 311$, (*h*) $t/(d^2/Q_0) = 363$, (*i*) $t/(d^2/Q_0) = 418$.

for $\tilde{t} \leqslant 100$, the match between the data and the model is not perfect because the experimental concentration profile adjusts partially due to the lack of self-similarity in the jet. We believe this issue is related to the zone of flow establishment discussed previously. Then, both the advection (location of the peak in time) and the dispersion (width of the curve) seem to agree. There is a consistent mismatch at the rear where the data seem to be more spread out. This is probably due to some residue of dye in the tube still being injected in the jet at late times, and apparently stretching and diffusing the experimental dye concentration. In fact, we can see in figure 18(*a*) that even after $\tilde{t} > \tilde{t}_{90}$ the total integrated dye concentration detected by the camera is still increasing. We further believe that for times greater than the time instant of the maximum of the curve plotted with pluses in figure 18(*a*) (i.e. approximately $\tilde{t} > 290$), more dye is released in the study area due to the Taylor dispersion in the nozzle tube though at a smaller rate than the dye being advected out of the study area by the jet. In our study we have decided to make the simplifying assumption that the

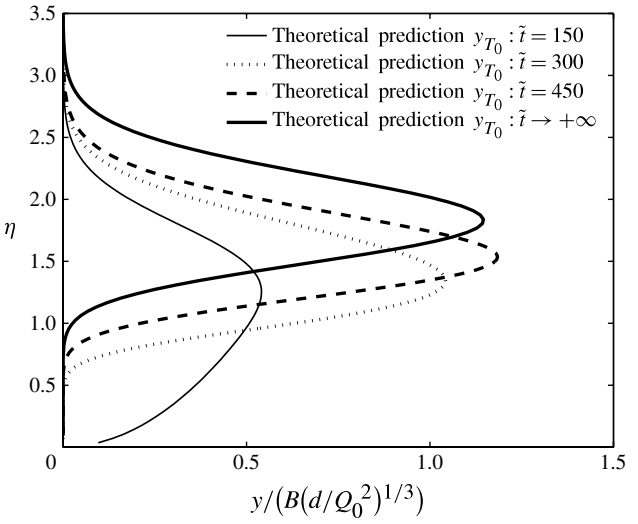

FIGURE 20. Finite-volume case, in similarity form. Plots of the variation with similarity variable $\eta = z/\left(t^{2/3}\left({Q_0}^2/d\right)\right)$ of the non-dimensionalized theoretical prediction y_{T_0}, based on (3.55), computed at $\tilde{t} = 150$ (thin solid curve), $\tilde{t} = 300$ (dotted curve), and $\tilde{t} = 450$ (dashed curve), using the reference advection and dispersion parameters $K_a = 1.65$ and $K_d = 0.09$, respectively, and the source function $f_{\tilde{t}_{90}}(t)$ as defined in (5.11). The asymptotic distribution of y_{T_0} (plotted with a thick solid curve) is equal to y_δ and can be computed using (3.44) with $K_a = 1.65$ and $K_d = 0.09$.

dye is released at a constant rate for a finite time: for $0 < \tilde{t} < \tilde{t}_{90}$. The time evolution of the total integrated concentration resulting from this assumption is plotted with a dotted curve in figure 18(*a*). We can see that this assumption does not perfectly model the experimental data (plotted with pluses in figure 18*a*). Therefore, we believe that the consistent late-time mismatch at the rear between the theoretical and experimental curves in figure 19 is simply due to the fact that our simplifying assumption does not take into account the delayed injection of the residual dye in the tank.

According to (3.56), the solution $\phi_{T_0}(z, t)$ converges in time towards $\phi_\delta(z, t)$. Hence, we also expect the data $\phi_{B,exp}(z, t)$ to converge in time towards $\phi_\delta(z, t)$. We demonstrate this convergence by plotting in figure 20 the similarity form of the theoretical prediction ϕ_{T_0} at $\tilde{t} = 150$ (plotted with a thin solid curve), $\tilde{t} = 300$ (plotted with a dotted curve) and $\tilde{t} = 450$ (plotted with a dashed curve). We also show the asymptotic solution y_δ, defined by (3.44) and computed using the reference advection and dispersion parameters $K_a = 1.65$ and $K_d = 0.09$. We can measure the absolute deviation, based on (3.58), between y_{T_0} at $\tilde{t} = 300$ when the integrated concentration of dye is approximately maximum (see figure 18*a*) and the asymptotic solution y_δ. We find dev $= 0.85$, computed for $\tilde{t}/\tilde{T}_0 = 300/183 \approx 1.64$ and using (3.58). If we consider that convergence is 'achieved' if dev $\leqslant 0.1$, then we find that our experimental data would be expected to achieve convergence for $\tilde{t}/\tilde{T}_0 \geqslant 13.6$, or at $\tilde{t} \geqslant 2488$. We can estimate that the distance at which we should observe the concentration distribution of the finite volumes of dye converge towards an asymptotic distribution is $z \geqslant \eta_a \left(13.6\tilde{T}_0\right)^{2/3} d \approx 2$ m, based on the location of the concentration peak at convergence. Finally, we can predict the key characteristics of y_δ, the asymptotic

distribution of $y_{B,exp}$ (the similarity form of $\phi_{B,exp}$ computed using (3.37)), which are actually identical to the characteristics of the theoretical prediction found for the virtual particles because the advection and dispersion parameters are the same. So, we can expect that the maximum concentration of the asymptotic distribution of $y_{B,exp}$ is located at $\eta_a = 1.83$, based on (3.24) with $K_a = 1.65$; the portion of the virtual particles which travels ahead of the advective front is $\beta_B = 0.54$ (shown with a cross in figure 6*a*), based on the ratio $K_d/K_a = 0.055$ and using (3.48); and the average location of the volume of tracers travelling ahead of the advective front is $\xi_B = 0.17$ (shown with a cross in figure 6*b*), based on the ratio $K_d/K_a = 0.055$ and using (3.50).

6. Conclusion

In this theoretical and experimental study, we have analysed the time-dependent transport and dispersion properties along the streamwise direction of quasi-two-dimensional jets. We model the evolution in time and space of the concentration of passive tracers using a one-dimensional time-dependent effective advection–diffusion equation. We integrate the concentration across the jet in order to be able to solve our proposed heuristic advection–diffusion (2.3). From the analysis of experimental results we find that this simplification appears to be appropriate, because the tracer distribution remains confined within the quasi-two-dimensional jet between two linearly-expanding straight-sided boundaries (Landel *et al.* 2012). Neglecting any molecular diffusion, we assume a streamwise turbulent eddy diffusion coefficient proportional to the product of the local half-width of the jet $b(z) \propto z$ and the local time-averaged maximum vertical velocity $\overline{w}_m(z) \propto z^{-1/2}$ (analogously to mixing length theory). The streamwise turbulent eddy diffusion coefficient models physically the interaction between the core and eddy structures of quasi-two-dimensional jets. (In Landel *et al.* (2012), we showed that the core–eddy structure was self-similar with height, with characteristic local length scale $b(z)$, and with characteristic local velocity scale $\overline{w}_m(z)$.)

Using a streamwise turbulent eddy diffusion coefficient scaling like ${M_0}^{1/2}z^{1/2}$, we are able to transform the effective advection–diffusion equation into a similarity form. We solve analytically the resulting ordinary differential equation in the cases of a constant-flux release and an instantaneous finite-volume release yielding a 'fundamental solution'. The solutions depend on two parameters, an advection parameter K_a and a dispersion parameter K_d, which we determine using experimental measurements. We also provide an integral formulation for the general problem of an arbitrary time-dependent release of tracers governed by a source function. The integral formulation for this more realistic case is the convolution between the fundamental solution found for the instantaneous finite-volume release and the source function. We present an analytical solution for the general problem in the case of a rectangular source function (i.e. the flux of tracers at the jet source is constant for a finite period of time, T_0, and zero otherwise, thus releasing a finite volume). At large time ($t \gg T_0$), this solution converges towards the fundamental solution found for the instantaneous finite-volume release. On the other hand, for $T_0 \to \infty$, this solution converges towards the solution found for the constant-flux release.

Furthermore, we show theoretically that, owing to dispersion mechanisms, a non-negligible portion of the total volume of tracers released travels ahead of the advective front, in both the finite-volume and the constant-flux cases. The advective front corresponds to the location of the tracers (in the finite-volume case) or the leading front of the tracer distribution (in the constant-flux case) if all dispersion mechanisms

are ignored, $K_d = 0$ and we assume a top-hat distribution for the velocity with no turbulent dispersion. Owing to the self-similarity form of the flow, we also find that the streamwise dispersion increases in time as $t^{2/3}$.

We compare the theoretical model with experimental measurements obtained by tracking the concentration of dye or virtual particles in time and space. We conduct both constant-flux and finite-volume releases of dye in quasi-two-dimensional steady turbulent jets. We also release finite volumes of virtual particles transported as passive tracers instantaneously in the fully resolved time-dependent velocity fields of quasi-two-dimensional steady turbulent jets. We consider the experimental data for constant-flux releases of dye more accurate because the initial, boundary and integral conditions imposed in the theoretical model are more straightforward to satisfy experimentally. We find that the experimental results agree well with the theoretical prediction, using either the horizontally-integrated concentration of dye ϕ or the streamwise concentration flux of dye M_ϕ as defined in (2.1) and (2.5*b*), respectively. The similarity scaling derived from the model $\eta \propto z/t^{2/3}$ is appropriate to study this phenomenon. We find that what we refer to as our 'reference' values for the advection and dispersion parameters are $K_a = 1.65$ and $K_d = 0.09$, respectively, determined from the study of the concentration in the constant-flux dye experiments.

We largely confirm these results by the complementary experimental data obtained with finite-volume releases of virtual particles. The data converge in similarity form towards the fundamental theoretical solution, assuming an instantaneous finite-volume release. The similarity scaling $\eta \propto z/t^{2/3}$ is also appropriate in this case. We find that the best fits to the advection and dispersion parameters are $K_a = 1.62$ and $K_d = 0.09$, respectively. In the case of finite-volume releases of dye, we find that the experimental concentration distribution has not converged towards the asymptotic fundamental solution, assuming an instantaneous release. We believe that this is principally due to the fact that the dye could not be released instantaneously in the experiment. The duration of the dye release introduces a new time scale T_0, which affects the concentration distribution. Until $t \gg T_0$, the concentration distribution is in a transition regime, which we model using the general model ϕ_{T_0} defined in (3.55), assuming a rectangular source function. We find that the best fits to the advection and dispersion parameters are $K_a = 1.75$ and $K_d = 0.09$, respectively. We also calculate that, in this case, the distribution should 'converge', the normalized absolute deviation between ϕ_{T_0} and ϕ_δ, defined in (3.58), is smaller than 0.1 towards the fundamental solution ϕ_δ defined in (3.44) after a duration equal to approximately 14 times the time of release of the dye (i.e. $t \geqslant 14T_0$). In other words, the dye distribution should converge towards an asymptotic distribution at $z \approx 2$ m, at a distance larger than four times the maximum distance of our study area.

Our model appears to be robust to variations in the initial boundary conditions of the experiments. In the experiments with finite-volume releases of virtual particles, even though the particles are released instantaneously but far away from the source, the particle concentration distribution seems to converge rapidly in time towards a stable asymptotic distribution predicted by the model. In the experiments with finite-volume releases of dye, even though the dye is released near the source but not instantaneously, we can prove that the dye concentration distribution will eventually converge in time towards a stable asymptotic distribution predicted by the model. Moreover, we can estimate the time before convergence and provide a model for the transition regime.

Overall, the model largely appears to agree with the data, especially at the dispersive front of the distribution. In table 1 we collect all the various key experimentally

Case	Theory	K_a	K_d	K_d/K_a	η_a	β	ξ
Constant-flux release (dye)	y_F	1.65	0.09	0.055	1.83	0.12–0.10	0.16–0.13
Constant-flux release (dye)	y_M	1.55	0.07	0.045	1.83	0.09–0.06	0.19–0.12
Instantaneous finite-volume release (virtual particles)	y_δ	1.62	0.09	0.056	1.83–1.83	0.49–0.54	0.13–0.17
Finite-volume release (dye)	ϕ_{T_0}	1.75	0.09	0.051	1.83[a]	0.54[a]	0.17[a]

TABLE 1. Summary of the key experimental results found in the constant-flux and the finite-volume cases. The values for the advection and dispersion parameters K_a and K_d are obtained from the best least-squares fit of the experimental data. On the other hand, η_a, β and ξ are computed theoretically using the 'reference' parameters $K_a = 1.65$ and $K_d = 0.09$, found in the constant-flux case; if two values are indicated, the first value is measured experimentally while the second value is computed theoretically using $K_a = 1.65$ and $K_d = 0.09$. [a] Theoretical value after ϕ_{T_0} converges to ϕ_δ.

determined quantities. By comparing the various models with all the experiments, we are able to give an estimated range for the advection and dispersion parameters. We find that the advection and dispersion parameters are $K_a = 1.65 \pm 0.10$ and $K_d = 0.09 \pm 0.02$ respectively, and the ratio between the two is within the range $0.045 \leqslant K_d/K_a \leqslant 0.056$. For both the constant-flux case and the instantaneous finite-volume case, the location in similarity space of the advective front (as defined in (3.24)) is found at $\eta_a = 1.83$. Then, in the case of constant-flux releases of tracers, we find that, at each instant in time, approximately $\beta_F = 11 \pm 1\,\%$ (as defined in (3.27)) of the total volume of tracers having already been released is transported ahead of the advective front, at an averaged normalized distance in similarity space $\xi_F = 0.145 \pm 0.015$ (as defined in (3.29)). In the case of an instantaneous finite-volume release of tracers, about $\beta_B = 51.5 \pm 2.5\,\%$ (as defined in (3.48)) of the total volume of tracers released is transported ahead of the advective front η_a, at an averaged normalized distance in similarity space $\xi_B = 0.15 \pm 0.02$ (as defined in (3.50)).

In § 1, we discussed the importance of modelling correctly the transport and dispersion of tracers in quasi-two-dimensional jet flows. We believe that the model developed in the present work provides not only a strong insight into these mechanisms but also a quantitative basis to predict them. Comparisons with experimental data obtained using different techniques support the predictions of the model. From this comparison, we can also measure accurately the strength of the advection and the strength of the dispersion in quasi-two-dimensional jets, using only an advection parameter K_a and a dispersion parameter K_d, respectively. Finally, we have discovered that the streamwise dispersion increases in time like $t^{2/3}$. In other words, a significant amount of tracers released in quasi-two-dimensional jets is transported faster than the speed predicted by a simple advection model. Such predictions are crucial to many applications, particularly in the event of environmental pollutions in rivers and lakes.

Acknowledgements

This work has been funded through the BP Institute (BPI) and EPSRC. We gratefully acknowledge the technical assistance and advice of Dr S. Dalziel (DAMTP). Thanks are also due to A. Pluck (BPI), and D. Page-Croft and the technicians of the

G. K. Batchelor Laboratory (DAMTP). This paper has been substantially improved by the thoughtful and constructive criticism of two anonymous reviewers.

Appendix. Proof of (3.56)

If $t > T_0$, we have, according to (3.55),

$$\phi_{T_0}(z,t) = \frac{K_{T_0}}{T_0} z^{1/2} \left(\int_{s(t)}^{+\infty} h^{a-1} \mathrm{e}^{-h}\, \mathrm{d}h - \int_{s(t-T_0)}^{+\infty} h^{a-1} \mathrm{e}^{-h}\, \mathrm{d}h \right), \tag{A 1}$$

with

$$K_{T_0} = \frac{2B}{3K_d {M_0}^{1/2} \Gamma\,[a+1]}, \quad a = \frac{2}{3}\left(\frac{K_a}{K_d} - \frac{1}{2}\right) \quad \text{and} \quad s(t) = \frac{4z^{3/2}}{9K_d {M_0}^{1/2} t}. \tag{A 2a–c}$$

Combining the two integrals, in the limit $t \gg T_0$, (A 1) becomes

$$\phi_{T_0}(z,t) \sim \frac{K_{T_0}}{T_0} z^{1/2} (s(t))^{a-1} \mathrm{e}^{-s(t)} \left(s(t-T_0) - s(t)\right) \tag{A 3}$$

$$\sim K_{T_0} \frac{z^{1/2}}{t} (s(t))^{a} \mathrm{e}^{-s(t)}. \tag{A 4}$$

Using $\eta = z/\left(t^{2/3} {M_0}^{1/3}\right)$, (A 2*b,c*), we obtain

$$\phi_{T_0}(z,t) \sim t^{-2/3} K_{T_0} {M_0}^{1/6} \left(\frac{4}{9K_d}\right)^{a} \eta^{K_a/K_d} \exp\left[-\frac{4}{9K_d}\eta^{3/2}\right]. \tag{A 5}$$

Finally, using (A 2*a*), we find

$$\phi_{T_0}(z,t) \sim t^{-2/3} \frac{B}{\left(\frac{3}{2}\right)^{2a+1} (K_d)^{a+1} \Gamma\,[a+1]\, {M_0}^{1/3}} \eta^{K_a/K_d} \exp\left[-\frac{4}{9K_d}\eta^{3/2}\right] \tag{A 6}$$

$$= t^{-2/3} y_\delta(\eta), \tag{A 7}$$

where y_δ is defined in (3.44), and hence (3.56) follows.

REFERENCES

CENEDESE, C. & DALZIEL, S. B. 1998 Concentration and depth fields determined by the light transmitted through a dyed solution. In *Proceedings of the 8th International Symposium on Flow Visualization* (ed. G. M. Carlomagno & I. Grant) ISBN 0 9533991 0 9, paper 061.

CHATWIN, P. C. & ALLEN, C. M. 1985 Mathematical models of dispersion in rivers and estuaries. *Annu. Rev. Fluid Mech.* **17**, 119–149.

CHEN, D. & JIRKA, G. H. 1998 Linear stability analysis of turbulent mixing layers and jets in shallow water layers. *J. Hydraul. Res.* **36**, 815–830.

CHEN, D. & JIRKA, G. H. 1999 LIF study of plane jet bounded in shallow water layer. *J. Hydraul. Engng* **125**, 817–826.

COOMARASWAMY, I. A. 2011 Natural ventilation of buildings: time-dependent phenomena. PhD thesis, University of Cambridge.

DALZIEL, S. B. 1992 Decay of rotating turbulence: some particle tracking experiments. *Appl. Sci. Res.* **49**, 217–244.

DALZIEL, S. B., PATTERSON, M. D., CAULFIELD, C. P. & COOMARASWAMY, I. A. 2008 Mixing efficiency in high-aspect-ratio Rayleigh–Taylor experiments. *Phys. Fluids* **20**, 065106.

DRACOS, T., GIGER, M. & JIRKA, G. H. 1992 Plane turbulent jets in a bounded fluid layer. *J. Fluid Mech.* **241**, 587–614.

DUTKIEWICZ, S., GRIFFA, A. & OLSON, D. B. 1993 Particle diffusion in a meandering jet. *J. Geophys. Res., Oceans* **98**, 16,487–16,500.

FISCHER, H. B. 1973 Longitudinal dispersion and turbulent mixing in open-channel flow. *Annu. Rev. Fluid Mech.* **5**, 59–78.

GIGER, M., DRACOS, T. & JIRKA, G. H. 1991 Entrainment and mixing in plane turbulent jets in shallow water. *J. Hydraul. Res.* **29**, 615–642.

GRADSHTEYN, I. S. & RYZHIK, I. M. 2007 *Table of Integrals, Series, and Products*, seventh edition. Elsevier.

JIRKA, G. H. 2001 Large scale flow structures and mixing processes in shallow flows. *J. Hydraul. Res.* **39**, 567–573.

JIRKA, G. H. & UIJTTEWAAL, W. S. J. 2004 Shallow flows: a definition. In *Shallow Flows* (ed. G. H. Jirka & W. S. J. Uijttewaal). pp. 3–11. Taylor & Francis.

LANDEL, J. R., CAULFIELD, C. P. & WOODS, A. W. 2012 Meandering due to large eddies and the statistically self-similar dynamics of quasi-two-dimensional jets. *J. Fluid Mech.* **692**, 347–368.

LAW, A. W. K. 2006 Velocity and concentration distributions of round and plane turbulent jets. *J. Engng Math.* **56**, 69–78.

LEWIS, R. 1997 *Dispersion in Estuaries and Coastal Waters*. Wiley.

LUO, K., KLEIN, M., FAN, J.-R. & CEN, K.-F. 2006 Effects on particle dispersion by turbulent transition in a jet. *Phys. Lett.* A **357**, 345–350.

MACCREADY, P. & GEYER, W. R. 2010 Advances in estuarine physics. *Annu. Rev. Mar. Sci.* **2**, 35–58.

MATHIEU, J. & SCOTT, J. 2000 *An Introduction to Turbulent Flow*. Cambridge University Press.

MORTON, B. R., TAYLOR, G. I. & TURNER, J. S. 1956 Turbulent gravitational convection from maintained and instantaneous sources. *Proc. R. Soc. Lond.* A **234**, 1–23.

NATIONAL INSTITUTE OF STANDARDS AND TECHNOLOGY (2012) *NIST Digital Library of Mathematical Functions*, version 2012-03-23. http://dlmf.nist.gov/.

PARANTHOËN, P., FOUARI, A., DUPONT, A. & LECORDIER, J. C. 1988 Dispersion measurements in turbulent flows (boundary layer and plane jet). *Intl J. Heat Mass Transfer* **31**, 153–165.

PICANO, F., SARDINA, G., GUALTIERI, P. & CASCIOLA, C. M. 2010 Anomalous memory effects on transport of inertial particles in turbulent jets. *Phys. Fluids* **22**, 051705.

PRANDTL, L. 1925 A report on testing for built-up turbulence. *Z. Angew. Math. Mech.* **5**, 136–139.

ROWLAND, J. C., STACEY, M. T. & DIETRICH, W. E. 2009 Turbulent characteristics of a shallow wall-bounded plane jet: experimental implications for river mouth hydrodynamics. *J. Fluid Mech.* **627**, 423–449.

SCHEFER, R. W., KERSTEIN, A. R., NAMAZIAN, M. & KELLY, J. 1994 Role of large-scale structure in a nonreacting turbulent CH4 jet. *Phys. Fluids* **6**, 652–661.

SVEEN, J. K. & DALZIEL, S. B. 2005 A dynamic masking technique for combined measurements of PIV and synthetic schlieren applied to internal gravity waves. *Meas. Sci. Technol.* **16**, 1954–1960.

TAYLOR, G. I. 1953 Dispersion of soluble matter in solvent flowing slowly through a tube. *Proc. R. Soc. Lond.* A **219**, 186–203.

TAYLOR, G. I. 1954 The dispersion of matter in turbulent flow through a pipe. *Proc. R. Soc. Lond.* A **223**, 446–468.

TURNER, J. S. 1986 Turbulent entrainment: the development of the entrainment assumption, and its application to geophysical flows. *J. Fluid Mech.* **173**, 431–471.

UBEROI, M. S. & SINGH, P. I. 1975 Turbulent mixing in a two-dimensional jet. *Phys. Fluids* **18**, 764–769.

WARD, P. R. B. & FISCHER, H. B. 1971 Some limitations on use of one-dimensional dispersion equation, with comments. *Water Res. Res.* **7**, 215.

YANG, Y., CROWE, C. T., CHUNG, J. N. & TROUTT, T. R. 2000 Experiments on particle dispersion in a plane wake. *Intl J. Multiphase Flow* **26**, 1583–1607.

YANNOPOULOS, P. & NOUTSOPOULOS, G. 1990 The plane vertical turbulent buoyant jet. *J. Hydraul. Res.* **28**, 565–580.